Controlling dephasing of coupled qubits via shared bath coherence

L. M. J. Hall,* L. S. Sirkina, A. Morreau, W. Langbein, and E. A. Muljarov†
School of Physics and Astronomy, Cardiff University, Cardiff CF24 3AA, United Kingdom

(Received 23 May 2024; revised 25 October 2024; accepted 9 June 2025; published 1 July 2025)

The interaction of a quantum system with its environment limits its coherence time. This, in particular, restricts the utility of qubits in quantum information processing applications. In this paper, we show that the decoherence of a coupled qubit system can be minimized, or even eliminated, by exploiting the quantum coherence of the bath itself. We investigate the dephasing in a system of two spatially separated, electronically decoupled qubits, with direct or mediated coupling, interacting with a shared bath. For illustration, we treat Förster or cavity-mediated coupling between semiconductor quantum dots interacting with acoustic phonons. Using the rigorous method of Trotter's decomposition with cumulant expansion, we demonstrate a reduction in the dephasing rates at specific distances between the dots. The control of dephasing with distance is a coherent effect of the shared bath and is absent for independent baths. It can be understood in terms of phonon-assisted transitions between the entangled qubit states of the coupled system.

DOI: 10.1103/ltk8-fpv3

I. INTRODUCTION

A quantum bit, or qubit, is a two-level quantum-mechanical system. While in many ways, the qubit is analogous to the classical binary bit, quantum computing infrastructure is unique in its reliance on coherent superposition of one or more qubits. Two-qubit logic gates, in particular, are a fundamental building block in any quantum computing architecture [1,2]. Such gates require a controlled long-range interaction between isolated qubits, which can be mediated by their strong coupling to a photonic cavity [3]. The lifetime of this interaction, known as the coherence time, dictates the complexity of calculations that can be achieved and the accuracy of the calculated results. Inevitably, the coupling of the qubits to their environment, often treated as a thermal bath, limits coherence times and hence restricts the practical application of multiqubit logic gates [4,5].

Historically, the dominating source of decoherence in a multiqubit system inside a cavity was due to the leakage of photons from the cavity due to its low quality factor, causing coupling with the continuum of external photonic modes. Therefore, previous works have focused on exploiting the photonic bath coherent properties to reduce dephasing, such as decoherence-free subspaces of subradiant quantum superpositions [6,7]. Specifically, the introduction of a second qubit coupled to the same cavity gives rise to a subradiant superposition state that is decoupled from the lossy cavity. Although the quality factor of optical cavities dramatically increased over the past decade, coherence times remain limited due to other facets of the environment, the details of which are specific to the physical implementation of the qubit system.

While there are many possible physical implementations of a qubit, we will focus here on semiconductor quantum dots (QDs), often referred to as "artificial atoms." They are a promising qubit candidate, since quantum interference of single photons emitted by spatially separated GaAs QDs has been experimentally demonstrated [8–10]. Coupling these QDs to optical cavities further enhances this effect [11] and maintaining this coherence is of great importance for applications in quantum computing. However, in semiconductor QDs, acoustic phonons present the major intrinsic source of decoherence. Even at low temperatures, acoustic phonons induce a rapid non-Markovian decay of the QD coherence [12,13], also known as a phonon broad band (BB) in the QD spectrum, followed by a nearly Markovian long-time decay of the zero-phonon line (ZPL) due to real or virtual phonon-assisted transitions to other QD levels [14,15].

The QD interaction with a phonon bath fundamentally differs from the bilinear QD-cavity coupling, so that the aforementioned idea of decoherence-free subspaces of qubit states is not directly applicable here. Nevertheless, progress has been made to reduce the effect of QD decoherence in qubit control. In particular, using a controlled off-resonant optical pulse with the laser pulse frequency tuned to the BB allows one to prepare almost pure qubit states by using phonon-assisted transitions [16,17]. Notably, this only applies in the low temperature regime, where phonon absorption can be reasonably neglected. The idea has been generalized to a phonon-assisted two-photon excitation scheme to create indistinguishable entangled photon pairs from remote QDs [18]. The Purcell effect helps to reduce the phonon-induced decoherence by a resonant weak coupling of a QD exciton to a cavity mode that results in reduction of the relative

*Contact author: Luke.Hall415@gmail.com
†Contact author: Egor.Muljarov@astro.cf.ac.uk

weight of the BB and enhancement of the ZPL emission [19]. Moreover, in the QD-cavity strong-coupling regime, the BB is almost entirely eliminated in the cavity excitation scheme [20,21]. However, the ZPL gains an additional dephasing [22] which can be understood and quantified in terms of phonon-assisted transitions between the polariton states of the system [23]. Such a ZPL dephasing can be enhanced in coupled qubits where all parts of the system are interacting with the bath.

In this paper, we demonstrate a reduction, or even a complete elimination, of the ZPL dephasing in a system of two QD qubits coupled to each other directly or via an optical cavity and interacting with a bath of acoustic phonons. We show that, while the interaction of the hybridized qubits with a shared environment usually causes dephasing of qubit states, the coherent properties of the bath can reduce this decoherence.

To enable an accurate treatment, we generalize the Trotter's decomposition with linked cluster expansion technique [23], which provides an asymptotically exact solution for the dynamics of spatially separated QD systems, capturing bath memory effects and non-Markovian behavior. This approach is compared with the approximate Fermi's golden rule calculations commonly used in earlier works, establishing the validity range of such an approximation. We consider a purely diagonal electron-phonon coupling, which produces no ZPL broadening within individual QDs. Our full calculation reveals ZPL broadening which can be understood in terms phonon-assisted transitions between the hybridized qubit states of the coupled QD system. We demonstrate, using the asymptotically exact calculation, a reduction of the ZPL dephasing in a system of two QD qubits coupled to each other directly or via an optical cavity and interacting with a three-dimensional (3D) bath of acoustic phonons. This suppression results from the collective coupling of the QD qubits to shared phonon modes [24], enabled by the extended coherence length of the bath states. In particular, when the QD separation is an integer multiple of the phonon wavelength, selected by the energy splitting of the coupled states, there is a reduction in the decoherence. We show that a near-vanishing dephasing rate, which can be referred to as a 1D regime, can be achieved by utilizing strong QD-cavity coupling strengths. We quantify the QD separations at which the 1D regime persists before transitioning to the expected 3D behavior, providing insights which are not present in earlier works. A distance-independent direct coupling is used as an illustration to be compared with results for cavity-mediated coupling which is a more realistic model for constant coupling strength across the considered separation range.

II. SYSTEM HAMILTONIAN

As a practical example, we consider the decoherence of electronically decoupled qubits separated by a distance d and interacting with a shared bath. The coupling of the qubits is taken as either direct through dipolar Förster-type coupling [25–28], indirectly via cavity-mediation [29–31], or both. As qubit and bath realization we use semiconductor QDs interacting with a bath of 3D acoustic phonons, widely studied in the literature [12–15,32].

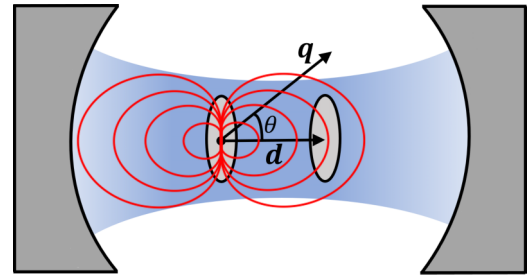

FIG. 1. Schematic of the system with a pair of dipole-coupled qubits separated by a distance vector **d**, coupled to an optical cavity, and interacting with three-dimensional acoustic phonons described by a wave vector **q** and angle θ.

The system Hamiltonian can be written as a sum of two exactly solvable parts,

$$H = H_0 + H_{\rm IB}, \tag{1}$$

where H_0 describes the coupling between the qubits and the cavity and $H_{\rm IB}$ is a generalized independent boson (IB) model Hamiltonian describing the coupling of the qubits to the shared environment. For the system of two remote QDs coupled to an optical cavity, illustrated in Fig. 1, H_0 takes the form (with $\hbar = 1$)

$$\begin{aligned} H_0 = {} & \Omega_1 d_1^\dagger d_1 + \Omega_2 d_2^\dagger d_2 + \Omega_C a^\dagger a + g(d_1^\dagger d_2 + d_2^\dagger d_1) \\ & + g_1(d_1^\dagger a + a^\dagger d_1) + g_2(d_2^\dagger a + a^\dagger d_2), \end{aligned} \tag{2}$$

where $d_j^\dagger$ is the fermionic exciton creation operator in QD j ($j = 1, 2$), $a^\dagger$ is the cavity photon creation operator, Ω_j (Ω_C) is the exciton (cavity photon) frequency, g is the coupling strength between the QD excitons, and g_j is the coupling between the exciton in QD j and the cavity photon. The IB model Hamiltonian describes the interaction of the QD excitons with a shared acoustic-phonon bath,

$$H_{\rm IB} = H_{\rm ph} + d_1^\dagger d_1 V_1 + d_2^\dagger d_2 V_2, \tag{3}$$

where

$$H_{\rm ph} = \sum_{\mathbf{q}} \omega_q b_{\mathbf{q}}^\dagger b_{\mathbf{q}} \quad \text{and} \quad V_j = \sum_{\mathbf{q}} \lambda_{\mathbf{q},j}(b_{\mathbf{q}} + b_{-\mathbf{q}}^\dagger) \tag{4}$$

are, respectively, the free phonon bath Hamiltonian and the QD coupling to the bath, where $b_{\mathbf{q}}^\dagger$ is the bosonic creation operator of a bulk phonon mode with the momentum **q** and frequency ω_q (denoting $q = |\mathbf{q}|$). The coupling of the exciton in QD j to the phonon mode **q** is given by the matrix element $\lambda_{\mathbf{q},j}$, which depends on the material parameters, exciton wave function, and position of the QD. Their explicit form for isotropic and anisotropic QDs is provided in Appendix A. For identical QD qubits separated by a distance vector **d**, the matrix elements satisfy the relation

$$\lambda_{\mathbf{q},2} = e^{i\mathbf{q}\cdot\mathbf{d}} \lambda_{\mathbf{q},1}. \tag{5}$$

III. ASYMPTOTICALLY EXACT SOLUTION

In the following, we focus on the linear optical response, which we call the linear polarization below, allowing us to

study the coherence of the system as a function of the distance between the qubits. The linear polarization of qubit j is defined as $P_{jk}(t) = \mathrm{Tr}\{\rho(t)d_j\}$, where $\rho(t)$ is the full density matrix. We assume that starting from the system ground state the qubit with index k is instantaneously excited at time $t = 0$. As has been derived in Ref. [23], the linear polarization can written as

$$P_{jk}(t) = \langle\langle j|\,\hat{U}(t)\,|k\rangle\rangle_{\mathrm{ph}}, \tag{6}$$

where $\hat{U}(t) = e^{iH_{\mathrm{ph}}t}e^{-iHt}$ is the time evolution operator and $\langle\ldots\rangle_{\mathrm{ph}}$ denotes the expectation value over all phonon degrees of freedom in thermal equilibrium. Here and below we use the basis states

$$|j\rangle = d_j^\dagger\,|0\rangle \quad \text{and} \quad |C\rangle = a^\dagger\,|0\rangle\,, \tag{7}$$

where $|0\rangle$ represents the vacuum state of the QD-cavity subsystem and $j = 1, 2$.

Taking advantage of the two exactly solvable parts of the Hamiltonian Eq. (1), we apply the method of Trotter's decomposition with cumulant expansion [23] summarized in the following section, allowing to take into account the effect of the phonon environment *exactly*.

A. Trotter's decomposition

The method of Trotter's decomposition with linked cluster expansion developed in Ref. [23] for exact calculation of the linear polarization of a single QD simultaneously coupled to a cavity and a phonon bath is applied here to the more general case of cavity-mediated coupling between the QDs (with the coupling constants g_1 and g_2) and their direct dipolar coupling (with the coupling constant g), as described by Eq. (2). We commence by splitting the time interval $[0, t]$, where t is the observation time, into N equal steps of duration $\Delta t = t/N = t_n - t_{n-1}$, where $t_n = n\Delta t$ represents the time at the n-th step. Trotter's theorem is then used to separate the time evolution of the two noncommuting operators, H_0 and H_{IB}. For sufficiently small Δt, we can assume independent evolution of the two exactly solvable components within each time step. In fact, applying Trotter's decomposition theorem, the time evolution operator $\hat{U}(t)$ can be written as

$$\hat{U}(t) = \lim_{N\to\infty} e^{iH_{\mathrm{ph}}t}(e^{-iH_{\mathrm{IB}}t/N}e^{-iH_0t/N})^N. \tag{8}$$

We now introduce two operators $\hat{M}$ and $\hat{W}$, which describe the dynamics due to H_0 and H_{IB}, respectively, each being analytically solvable. Using these operators, the QD-cavity dynamics over a single time step is described by

$$\hat{M}(t_n - t_{n-1}) = \hat{M}(\Delta t) = e^{-iH_0\Delta t} \tag{9}$$

and the exciton-phonon dynamics is given by

$$\hat{W}(t_n, t_{n-1}) = e^{iH_{\mathrm{ph}}t_n}e^{-iH_{\mathrm{IB}}\Delta t}e^{-iH_{\mathrm{ph}}t_{n-1}}. \tag{10}$$

Exploiting the commutativity of H_0 and H_{ph}, one can write the time evolution operator Eq. (8) as

$$\hat{U}(t) = \mathcal{T}\prod_{n=1}^{N}\hat{W}(t_n, t_{n-1})\hat{M}(t_n - t_{n-1}), \tag{11}$$

where $\mathcal{T}$ is the time-ordering operator. $\hat{W}$ and $\hat{M}$ are both 3×3 matrices in the $|1\rangle$, $|2\rangle$, $|C\rangle$ basis, and, due to the diagonal form of the exciton-phonon interaction, $\hat{W}$ is diagonal. Its diagonal matrix elements can be written as

$$W_{i_n}(t_n, t_{n-1}) = \mathcal{T}\exp\left\{-i\int_{t_{n-1}}^{t_n}\tilde{V}_{i_n}(\tau)d\tau\right\}, \tag{12}$$

where

$$\tilde{V}_{i_n}(\tau) = \xi_{i_n}V_1(\tau) + \eta_{i_n}V_2(\tau) \tag{13}$$

for τ within the time interval $t_{n-1} \leqslant \tau \leqslant t_n$, with ξ_i and η_i being the components of the vectors $\vec{\xi} = (1, 0, 0)$ and $\vec{\eta} = (0, 1, 0)$, respectively, and $V_j(\tau) = e^{iH_{\mathrm{ph}}\tau}V_je^{-iH_{\mathrm{ph}}\tau}$ is the exciton-phonon coupling in the interaction representation, with V_j defined in Eq. (4). We use the indices i_n to indicate which state the system takes at a given time step n, being either $|1\rangle$, $|2\rangle$, or $|C\rangle$, with i_n taking the values 1, 2, or C, respectively. The elements of $\vec{\xi}$ and $\vec{\eta}$ selected by i_n determine the exciton-phonon coupling used during the n-th time step. For example, if the system is in the first QD exciton state during the n-th time step, then $i_n = 1$, and the exciton-phonon interaction V_1 occurs.

To find the polarization, we use Eq. (11) to substitute $\hat{U}(t)$ in Eq. (6) and write the matrix products explicitly, yielding

$$P_{jk}(t) = \sum_{i_{N-1}=1,2,C}\cdots\sum_{i_1=1,2,C}M_{i_Ni_{N-1}}\ldots M_{i_1i_0} \times \langle W_{i_N}(t, t_{N-1})\ldots W_{i_1}(t_1, 0)\rangle_{\mathrm{ph}}, \tag{14}$$

where $i_0 = k$ and $i_N = j$ denote, respectively, the excitation channel k at $t = 0$ and measurement channel j at the final time step $t_N = t$, and $M_{i_ni_m} = [\hat{M}(\Delta t)]_{i_ni_m}$. The W_{i_n} operators include the phonon contributions, and therefore we separate this product from the rest of the expression in order to take the expectation value and apply the linked cluster theorem [14,15,33].

B. Linked cluster expansion

To calculate the expectation value of the products of the exciton-phonon interaction operators in Eq. (14), we apply the linked cluster theorem. It allows us to write this expectation value as an exponential with a double sum over all possible second-order cumulants in the exponent [23,33],

$$\langle W_{i_N}(t, t_{N-1})\ldots W_{i_1}(t_1, 0)\rangle_{\mathrm{ph}} = \exp\left(\sum_{n=1}^{N}\sum_{m=1}^{N}\mathcal{K}_{i_ni_m}(|n-m|)\right) \tag{15}$$

with the cumulants in Eq. (15) given by

$$\mathcal{K}_{i_ni_m}(s) = -\frac{1}{2}\int_{t_{n-1}}^{t_n}d\tau_1\int_{t_{m-1}}^{t_m}d\tau_2\left\langle\mathcal{T}\tilde{V}_{i_n}(\tau_1)\tilde{V}_{i_m}(\tau_2)\right\rangle_{\mathrm{ph}}, \tag{16}$$

where $s = |n - m|$. Using Eq. (13), this cumulant can be expressed as

$$\mathcal{K}_{i_ni_m}(s) = \xi_{i_n}\xi_{i_m}K_{11}(s) + \eta_{i_n}\eta_{i_m}K_{22}(s) + (\xi_{i_n}\eta_{i_m} + \eta_{i_n}\xi_{i_m})K_{12}(s), \tag{17}$$

where we have introduced the cumulant elements

$$K_{jj'}(s) = -\frac{1}{2}\int_{t_{n-1}}^{t_n}d\tau_1\int_{t_{m-1}}^{t_m}d\tau_2D_{jj'}(\tau_1 - \tau_2), \tag{18}$$

having the symmetry $K_{jj'}(s) = K_{j'j}(s)$. Here we use the phonon Green's function

$$D_{jj'}(t) = \int_0^\infty d\omega\, J_{jj'}(\omega) D(\omega, t), \tag{19}$$

in which

$$J_{jj'}(\omega) = \sum_{\mathbf{q}} \lambda_{\mathbf{q},j} \lambda^*_{\mathbf{q},j'} \delta(\omega - \omega_q) \tag{20}$$

is the phonon spectral density and

$$D(\omega, t) = [\mathcal{N}_\omega + 1] e^{-i\omega|t|} + \mathcal{N}_\omega e^{i\omega|t|} \tag{21}$$

is the phonon propagator, where $\mathcal{N}_\omega = [e^{\omega/T} - 1]^{-1}$ is the Bose distribution function and T is the temperature (using units with the Boltzmann constant $k_B = 1$). The explicit analytical forms of the spectral density $J_{jj'}(\omega)$ for isotropic and anisotropic QDs are derived in Appendix A. The cumulant elements Eq. (18) can be conveniently expressed as linear combinations of the values on the time grid of the cumulant function

$$C_{jj'}(t) = -\frac{1}{2} \int_0^t d\tau_1 \int_0^t d\tau_2\, D_{jj'}(\tau_1 - \tau_2), \tag{22}$$

as detailed in Appendix B.

The linear polarization then takes the form given by Eqs. (14), (15), and (17). Note that a particular realization or a path of the system evolution is indicated by the indices $i_1, i_2, \ldots i_{N-1}$ in Eq. (14). However, to obtain the full quantum dynamics of the system, all possible realizations are to be summed over, in line with the path integral formalism. Technically this means a summation over all of the indices, which is done in Eq. (14).

C. The *L*-neighbor (*LN*) approach

For a finite bath memory time, it is sufficient to consider only a portion of the grid at least up to the memory time, which is referred to as the number of neighbors L, defined as the maximum value of $|n - m|$ taken into account in the calculation. The LN approach is used to describe the temporal correlations between all considered steps within the memory kernel. We first define a quantity $F^{(n)}_{i_L \ldots i_1}$ which is generated via the recursive relation

$$F^{(n+1)}_{i_L \ldots i_1} = \sum_{l=1,2,C} \mathcal{G}_{i_L \ldots i_1 l} F^{(n)}_{i_{L-1} \ldots i_1 l}, \tag{23}$$

using $F^{(1)}_{i_L \ldots i_1} = M_{i_1 k}$ as the initial value, where k is the excitation channel and $\hat{M}$ is given by Eq. (9). $\mathcal{G}$ is known as the propagator and is given by

$$\mathcal{G}_{i_L \ldots i_1 l} = M_{i_1 l} e^{\mathcal{K}_{ll}(0) + 2\mathcal{K}_{i_1 l}(1) + 2\mathcal{K}_{i_2 l}(2) + \cdots + 2\mathcal{K}_{i_L l}(L)} \tag{24}$$

with a more explicit form provided in Appendix B. The propagator $\mathcal{G}$ is a memory kernel containing the information required to propagate the system over a single time step. It includes the path segments connecting the current time interval with the L-nearest intervals and to itself which are shown by the L-shaped black outlined in Fig. 2. Each element of the tensor corresponds to a particular path of the system evolution within its memory. The linear polarization is then given by

$$P_{jk}(t) = e^{\mathcal{K}_{jj}(0)} F^{(N)}_{C \ldots C j}, \tag{25}$$

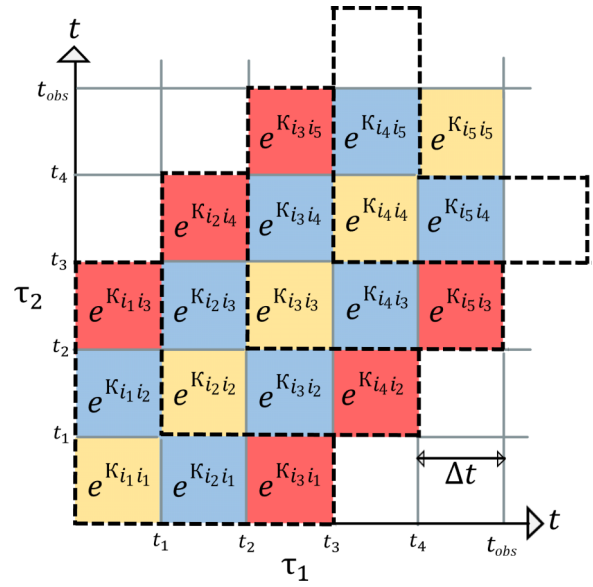

FIG. 2. A portion of the time grid used in the LN approach with $L = 2$, showing the self-interaction (yellow squares), the nearest, (blue squares) and next-nearest-neighbor interactions (red squares).

where j is the measurement state. The indices being placed in the cavity (C) state have the result of removing the excess contributions from the $\mathcal{G}$ tensor after the observation time t (see Fig. 2), as being in the cavity state reduces the cumulant at the corresponding times steps to zero. Equation (25) provides an asymptotically ($L \to \infty$) exact solution for the linear polarization. In practice, we calculate the linear polarization for a set of finite but sufficiently large L, up to $L = 30$ in this work, and extrapolate the result to $L \to \infty$ (see Appendix G for details on the extrapolation), in this way approaching the exact solution. This method can be generalized to other elements of the density matrix, such as the four-wave mixing polarization [21] and the population [34].

D. Independent phonon baths

The case of independent phonon baths can be considered as a simplification to the system, described by Eqs. (1)–(4) where the relevant modifications to the system Hamiltonian are applied to the H_{IB} term,

$$H_{\mathrm{IB}} = H_{\mathrm{ph},1} + H_{\mathrm{ph},2} + d_1^\dagger d_1 V_1 + d_2^\dagger d_2 V_2, \tag{26}$$

which now describes the interaction of each exciton with its own independent phonon bath, given in a similar way to Eq. (4) by

$$H_{\mathrm{ph},j} = \sum_{\mathbf{q}} \omega_{q,j} b^\dagger_{\mathbf{q},j} b_{\mathbf{q},j}, \quad V_j = \sum_{\mathbf{q}} \lambda_{\mathbf{q},j} (b_{\mathbf{q},j} + b^\dagger_{-\mathbf{q},j}). \tag{27}$$

Initially this may seem like a complication due to the extra terms. However, the resulting cumulant $\mathcal{K}_{i_n i_m}$ in Eq. (15) is nonvanishing only when $i_n = i_m$, i.e., the phonon Green's functions D_{12} and D_{21} corresponding to the cross terms vanish,

$$\langle \mathcal{T} \tilde{V}_1(\tau_1) \tilde{V}_2(\tau_2) \rangle = \langle \mathcal{T} \tilde{V}_2(\tau_1) \tilde{V}_1(\tau_2) \rangle = 0. \tag{28}$$

This is because the phonon operators in V_1 commute with those in V_2. The result is that the cumulant contains only the diagonal elements $K_{jj}(s)$, giving

$$\mathcal{K}_{i_n i_m}(s) = \begin{cases} \xi_{i_n}^2 K_{11}(s) + \eta_{i_n}^2 K_{22}(s) & i_n = i_m \\ 0 & i_n \neq i_m \end{cases}, \tag{29}$$

where $s = |n - m|$. The linear polarization in this case is calculated using Eqs. (23)–(25) with the modified cumulant elements Eq. (29).

IV. CONTROL OF DECOHERENCE

For illustration, we consider two cases: *Case A*, where the two qubits are directly coupled with strength g but do not interact with the cavity ($g_1 = g_2 = 0$), and *Case B*, where the qubits have no direct coupling ($g = 0$) but interact indirectly through the cavity, mediated by g_1 and g_2. To elucidate the effect of the shared environment on system coherence and its dependence on the interqubit distance $d = |\mathbf{d}|$, we assume that the coupling constants g_1, g_2, and g are distance independent. In a realistic system, Case A would exhibit a distance-dependent interaction between the QDs, such as Förster or tunnel coupling. However, we adopt a distance-independent coupling here to aid understanding Case B, where the cavity mediates the interaction between the QDs, providing a practical way to achieve coupling which is maintained for separations on the optical wavelength scale of a few 100 nm.

We assume without loss of generality that the first QD is instantaneously excited (e.g., by an ultrashort optical pulse), creating an excitonic polarization with $P_{jk}(0) = \delta_{jk}\delta_{k1}$, where δ_{jk} is the Kronecker delta.

A. Directly coupled QD qubits

1. Linear polarization and dephasing rates

In Case A, the time evolution of $P_{11}(t)$ for a system of two dipolar-coupled ($g = 0.5$ meV) identical isotropic QDs of confinement length $l = 5.6$ nm separated by the center-to-center distance $d = 5$ nm is shown in Fig. 3(a) by a blue dotted line, exhibiting decay and oscillations. The phonon bath parameters are taken as $D_c - D_v = -6.5$ eV, where D_c (D_v) is the conduction (valence) band deformation potential, $v_s = 4.6 \times 10^3$ m/s is sound velocity, $\rho_m = 5.65$ g/cm^3 is the mass density [14,15], and the temperature is $T = 20$ K.

The behavior in Fig. 3(a) is qualitatively explained by the energy level diagram in the right inset, showing hybridized states $|\pm\rangle = (|1\rangle \pm |2\rangle)/\sqrt{2}$ of the two-qubit coupled system at zero detuning ($\Omega_1 = \Omega_2$), where $|1\rangle$ and $|2\rangle$ are the individual QD excited states. The energy levels are separated by the Rabi splitting $2g$ determining the beat frequency in $|P_{11}(t)|$ which physically expresses the quantum information exchange between the qubits. The temporal decay of the linear polarization expresses the decoherence in this two-qubit system as a consequence of the interaction of the qubits with the bath. For these QD qubits, the decoherence is due to phonon-assisted transitions between the hybridized states.

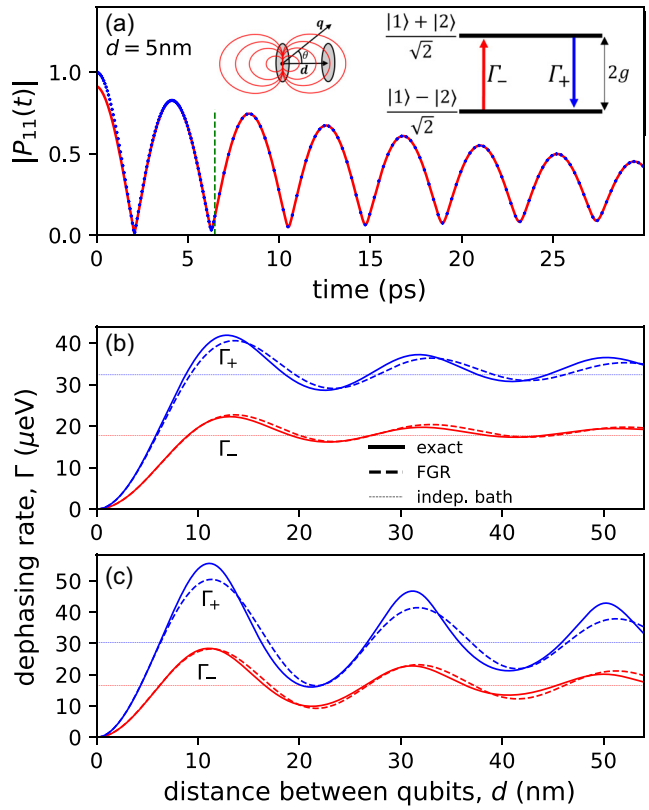

FIG. 3. (a) Linear optical polarization $P_{11}(t)$ (blue dots) and its complex biexponential fit (red lines) for dipolar coupled ($g = 0.5$ meV) isotropic QD qubits (left inset) at zero detuning, separated by the distance $d = 5$ nm, with excitation and measurement in QD 1. Right inset: Energy level diagram for the hybridized qubit states, with real phonon-assisted transitions (red and blue arrows). [(b) and (c)] Dephasing rates $\Gamma_\pm$ of the hybridized states $|\pm\rangle$ as a function of d, calculated exactly (solid lines) and via FGR (dashed lines) for (b) isotropic QDs with a confinement length of $l = 5.6$ nm and (c) anisotropic QDs with $l = 7.5$ nm across and $l_\perp = 2.5$ nm along the separation (see Appendixes A 1 and A 2 for details of isotropic and anisotropic QD models, respectively). The rates for independent phonon baths are shown by thin dashed horizontal lines. The phonon bath parameters are given in the main text.

With this picture in mind, we have applied to the long-time dynamics of $P_{11}(t)$ a biexponential fit of the form

$$P_{11}^{\text{fit}}(t) = \sum_j C_j e^{-i\omega_j t}, \tag{30}$$

extracting the complex amplitudes C_j, energies $\text{Re}\,\omega_j$, and dephasing rates $\Gamma_j = -\text{Im}\,\omega_j$ of the phonon-dressed hybridized states. The fit, applied after the phonon-memory cutoff [introduced in Appendix C by analyzing the cumulant functions and shown in Fig. 3(a) by the vertical dashed green line], demonstrates a remarkable agreement with the full calculation with a relative error below 10^{-10}. At earlier times the deviation is due to the formation of a polaron cloud around the optically excited QD, which is responsible for non-Markovian dephasing and the BB [13,21,23]. The dephasing rates Γ_j extracted from the fit as functions of the QD separation d are shown by solid lines in Fig. 3(b) for isotropic and in Fig. 3(c) for anisotropic

QDs. They are the dephasing rates of the states $|\pm\rangle$, denoted by $\Gamma_\pm$, and can be understood as being due to phonon-assisted transitions between the states. At short distances we observe a dramatic increase of the dephasing rates from zero at zero distance (which cannot be practically realized due to the finite extension of the QDs), followed by an oscillatory behavior at larger distances. Importantly, the minima of these dephasing rates are lower than the rates for independent baths (thin horizontal lines), due to collective coupling of the QD qubits to the same phonon modes, for distances less than the phonon coherence length.

2. *Phonon-assisted transitions between hybridized qubit states*

To understand the dependence on the distance between the qubits, we introduce the fermionic operators

$$p_\pm^\dagger = D_\mp d_1^\dagger \pm D_\pm d_2^\dagger, \tag{31}$$

creating excitations of the hybridized QD qubit states

$$|\pm\rangle = D_\mp|1\rangle \pm D_\pm|2\rangle, \tag{32}$$

where

$$D_\pm = \sqrt{(1 \pm \Delta/R)/2}, \tag{33}$$

with

$$\Delta = \Omega_2 - \Omega_1 \quad \text{and} \quad R = \sqrt{\Delta^2 + 4g^2} \tag{34}$$

being, respectively, the detuning and the Rabi splitting. In the absence of the bath, these operators diagonalize the system Hamiltonian Eq. (2) exactly:

$$H_0 = \Omega_+ p_+^\dagger p_+ + \Omega_- p_-^\dagger p_-, \tag{35}$$

where

$$\Omega_\pm = \frac{\Omega_1 + \Omega_2 \pm R}{2} \tag{36}$$

are the energies of the hybrid states $|\pm\rangle$.

Now applying this canonical transformation to the total Hamiltonian Eq. (1) we obtain

$$\begin{aligned} H = {} & (\Omega_+ + V_+) p_+^\dagger p_+ + (\Omega_- + V_-) p_-^\dagger p_- \\ & + V(p_+^\dagger p_- + p_-^\dagger p_+) + H_{\rm ph}, \end{aligned} \tag{37}$$

where $V_\pm = D_\mp^2 V_1 + D_\pm^2 V_2$ and $V = D_+ D_- (V_1 - V_2)$. The major outcome of this transformation is that the formerly diagonal interaction with the bath $H_{\rm IB}$, given by Eq. (3), now develops the off-diagonal elements $V(p_+^\dagger p_- + p_-^\dagger p_+)$ which enable phonon-assisted transitions between the hybridized qubit states. The transition rates can be evaluated via Fermi's golden rule (FGR) [15,23]:

$$\Gamma_- = \mathcal{N}_R\, \Gamma_{\rm ph}, \quad \Gamma_+ = (\mathcal{N}_R + 1)\, \Gamma_{\rm ph}, \tag{38}$$

where $\mathcal{N}_R$ is the Bose function taken at the Rabi splitting R and

$$\Gamma_{\rm ph} = \pi \sum_{\mathbf{q}} |D_+ D_- (\lambda_{\mathbf{q},1} - \lambda_{\mathbf{q},2})|^2 \delta(v_s q - R), \tag{39}$$

according to the off-diagonal coupling in Eq. (37). Here the delta function expresses the energy conservation in real transitions, indicating that the energy difference between the hybridized states should exactly match the energy of an emitted or absorbed phonon $\omega_q = v_s q$. The rate $\Gamma_{\rm ph}$ is evaluated in Appendix D, providing for an isotropic model of the QDs the explicit analytical result:

$$\Gamma_{\rm ph} = \Gamma_0 \left(1 - \frac{\sin(Rd/v_s)}{Rd/v_s}\right), \tag{40}$$

where $\Gamma_0 = D_+^2 D_-^2 R^3 (D_c - D_v)^2/(2\pi \rho_m v_s^5) e^{-l^2 R^2/v_s^2}$. The corresponding FGR calculation for an anisotropic model of the QDs is provided in Appendix D 2.

The FGR dephasing rates Eq. (40) are shown in Fig. 3(b) as dashed lines, reproducing the main features of the exact calculation but showing discrepancies (within 5%) due to multiphonon processes not present in FGR. The single-phonon transitions dominate at short distances as it is clear from the excellent agreement between the two results.

3. *Physical interpretation of decoherence reduction*

The initial quadratic growth with distance, the oscillations, and the reduction of $\Gamma_\pm$ at certain distances, seen in Fig. 3(b), are all caused by the coherent properties of the phonon bath. This coherence may be affected, for example, by higher-order phonon interactions (e.g., cubic interactions in Ref. [35]) which result in a finite phonon coherence time and thus a finite coherence length. While we do not consider this explicitly, we can distinguish two regimes: (i) The dot separation is less than the phonon coherence length, and thus the QDs can experience the same coherent phonon field and the collective coupling to the bath leads to the oscillations in our plots. (ii) The QD separation is larger than the coherence length, in which case the QDs do not interact with the same phonon modes, similarly to the independent bath calculation.

According to Eq. (37), the phonon-assisted coupling between the hybridized qubit states is given by $V_1 - V_2$ which is proportional to $1 - e^{i\mathbf{q}\cdot\mathbf{d}}$ [see Eq. (5)] and is vanishing at $\mathbf{q}\cdot\mathbf{d} = 2\pi n$, where n is an integer. This does not lead to a vanishing dephasing though, apart from $d = 0$, owing to the 3D nature of the phonon momentum $\mathbf{q}$ of the bath modes. However, as we show in Appendix D, in a 1D model of phonons with the same dispersion and same coupling, the dephasing rate Eq. (40) would modify to just

$$\Gamma_{\rm ph} = \Gamma_0 \left(\frac{v_s}{Rl}\right)^2 \sin^2\left(\frac{Rd}{2v_s}\right), \tag{41}$$

strictly vanishing at $Rd/v_s = 2\pi n$ for all n. To understand this phenomenon in 1D, let us take the two-qubit state just before the event of phonon emission or absorption as a superposition $\alpha|1\rangle + \beta|2\rangle$ with some complex amplitudes α and β. Since the qubits are in a hybridized state, they coherently emit or absorb the same phonon. This changes their phases (which is the source of pure dephasing) by φ_1 and φ_2, respectively, so that the two-qubit wave function becomes $\alpha e^{i\varphi_1}|1\rangle + \beta e^{i\varphi_2}|2\rangle$, with $\varphi_2 - \varphi_1 = \pm qd$, according to Eq. (5) and energy conservation requiring $R = v_s q$. Notably, if the separation d between the qubits is such that the phase difference is a multiple of 2π, i.e., $Rd/v_s = 2\pi n$ for an integer n, then the resulting wave function only acquires a common phase factor $e^{i\varphi_1}$, which is not changing the state. However, in order for the transition to occur between the initial and final states [e.g., between $|+\rangle$

and $|-\rangle$, see the inset in Fig. 3(a)], which would result in a phonon-induced dephasing, a change of the two-qubit state is required, meaning that the interaction with a phonon must induce a relative phase shift, i.e., $Rd/v_s \neq 2\pi n$.

Early papers revealed similar oscillatory behavior of the transition rates with distance in systems of spatially separated tunnel coupled QDs [24,36]. However, these are calculated approximately, using off-diagonal coupling between electronic states within the same QD, which is known to lead to long-time decoherence [14]. Reference [37] showed spatial correlations strongly influenced the quantum coherent transfer of excitations between biomolecular chromophores; however, the model is using distance-independent dipolar coupling and did not focus on the oscillatory behavior of the dephasing rates with distance. When considering more realistic couplings which decrease rapidly with distance, e.g., Förster coupled QDs in Ref. [27], or the tunnel coupling in Ref. [38], the oscillations disappear. There are also further studies which look at the distance dependence of exciton and spin QD qubits that reveal no oscillations [39]. Our work uses a distance-independent direct coupling as a simple illustration but further introduces a cavity-mediated coupled system as a more realistic model to facilitate distance-independent strong coupling.

Note that in the case of, e.g., nanowire-based QDs [40] or QDs in carbon nanotubes [41,42], the phonon dispersion and coupling are altered when the dimensionality is reduced from a bulk system. Several branches of phonon modes arise due to the reduced dimensionality and phonon quantization which are not present in 3D systems. This leads to changes in the phonon dispersion and coupling matrix elements. As a result, there is a finite zero-phonon linewidth which is not observed in QDs coupled to bulk phonons, where the linewidth remains zero in the ideal case. Here the ideal case corresponds to the condition $qd = 2\pi n$, for which no broadening of the ZPL is observed, due to the phonon interactions not facilitating a change of state, making the system effectively equivalent to the independent boson model [33] in which there is no ZPL broadening.

4. Anisotropic QD qubits

For 3D phonons and spherical QDs, the dephasing is absent only at $d = 0$ and according to Eq. (40) and Fig. 3(b) has minima around $Rd/v_s = 2\pi n + \pi/2$ ($n = 1, 2, \ldots$). The $\pi/2$ phase shift compared to the 1D case and nonvanishing dephasing at the minima are due to phonons of energy R that are absorbed or emitted at different angles θ to the QD separation vector $\mathbf{d}$ (Fig. 1), resulting in a variation of their phase difference $\varphi_2 - \varphi_1$ between the QDs. However, the reduction of decoherence is enhanced in anisotropic QDs, playing the role of directional phonon emitters or absorbers [43]. In fact, in oblate QDs separated along their short axis [Fig. 3(c)], directional coupling of phonons along the short axis effectively makes the system 1D under certain conditions.

Notably, in earlier studies, e.g., Refs. [24,36], the influence of the 3D bath is not obvious because the models are using a very strong anisotropy. Consequently, the studies are in a 1D-like regime, with little insight into the transition between 1D and 3D regimes. A follow-up work of Ref. [24] discussed the loss of the 1D regime by changing the effective mass in their system [44], which is reducing the confinement length in the in-plane parabolic confining potentials for electrons. Similarly, models with spherical QDs or weaker anisotropy yield finite dephasing rates across all separations, as seen from our calculation in Fig. 3, reflecting the influence of the 3D bath.

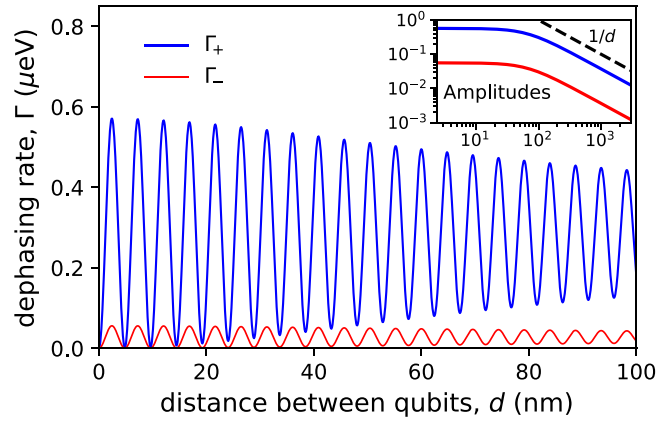

FIG. 4. As Fig. 3(c) but for $g = 2$ meV and FGR only (solid lines). Inset: Amplitude of the oscillations in the dephasing rates versus distance.

The dephasing rates for anisotropic QDs, calculated via FGR in Appendix D have a compact analytical expression Eq. (D9) in terms of the Faddeeva function, reproduce the main features of the exact calculation (with a relative difference below 7%), as seen in Fig. 3(c). In this case $l \gg l_\perp$, where l and $l_\perp$ are, respectively, the in-plane and perpendicular (along $\mathbf{d}$) exciton localization lengths, so that for $d \ll 2l^2q$, where $q = R/v_s$, the dephasing rates vanish at $qd = 2\pi n$, as it is clear from Eq. (A30) in Appendix A 3. If additionally $ql \gg 1$, meaning that the relevant phonon wavelength is small enough to create a directional emission, then the FGR dephasing rates reduce to Eq. (41). Under these conditions, the 3D system behaves as a 1D system, however, as the dot separation is increased, the 3D nature gradually returns. Furthermore, the 1D regime can be extended by increasing the anisotropy or increasing the energy R of the dominant phonon modes which couple to the system.

In fact, the analogy with pure 1D phonons becomes striking for stronger coupled QDs ($g = 2$ meV) as shown in Fig. 4, where the shorter phonon wavelength involved in transitions provides fast oscillations versus d, allowing for minima at short distances with near-vanishing dephasing. With such coupling strengths, the aforementioned condition $ql \gg 1$ is met, having a value $ql = 10$. The scaling of the oscillation amplitude with distance, given in the inset, demonstrates the quasi-1D behavior (shown by constant amplitude) for $d \ll 2l^2q \approx 148$ nm. This is consistent with the first few minima in the main plot having visually very small dephasing rates before gradually returning to the 3D regime as the dot separation increases. For this directional emission of phonons, the phonon Rayleigh length, given by $d_R = l^2q/2 \approx 37$ nm, estimates how far the phonons can propagate as a collimated Gaussian beam, maintaining 1D-like behavior. Beyond this distance, the system gradually transitions back to 3D. For 1D

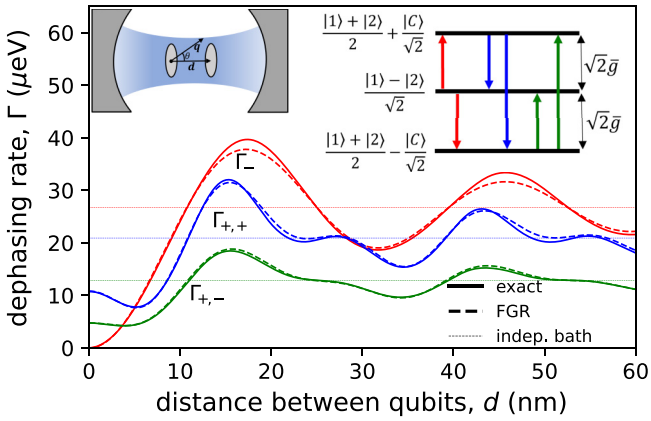

FIG. 5. Dephasing rates $\Gamma_{+,\pm}$ and Γ_- of the hybridized states as a function of d. Calculated exactly (solid lines) and via FGR (dashed lines) for cavity-mediated coupled anisotropic qubits (left inset) with interaction strength $g_1 = g_2 = \bar{g} = 0.5$ meV, and zero detuning. The dephasing rates for independent phonon baths are shown by thin dashed horizontal lines. Right inset: Energy level diagram for the hybridized qubit-cavity states $|+,\pm\rangle = (|1\rangle + |2\rangle)/2 \pm |C\rangle/\sqrt{2}$ and $|-\rangle = (|1\rangle - |2\rangle)/\sqrt{2}$, with real phonon-assisted transitions (red, blue and green arrows). Other parameters as in Fig. 3(c).

behavior to persist, the condition on the qubit separation then becomes $d \ll 4d_R$, where d_R serves as an approximate upper limit for ensuring the system remains in the 1D regime.

B. Cavity-mediated coupled QD qubits

In Case B of QDs indirectly coupled via a cavity, the dephasing is also controlled by collective coupling to the shared bath, though in a more complex scenario. For zero detuning ($\Omega_1 = \Omega_2 = \Omega_C$) and equal QD-cavity couplings ($g_1 = g_2 = \bar{g}$), the resulting three coupled states, $|+,\pm\rangle = (|1\rangle + |2\rangle)/2 \pm |C\rangle/\sqrt{2}$ and $|-\rangle = (|1\rangle - |2\rangle)/\sqrt{2}$, require a triexponential fit of $P_{11}(t)$ to extract the dephasing rates $\Gamma_j = -\mathrm{Im}\,\omega_j$, which are shown in Fig. 5 across a range of distances; see Appendix F for details of the fit. We observe oscillations versus distance d, different from those of directly coupled QDs (Fig. 3) since there are two periods contributing to the dephasing rates $\Gamma_{+,\pm}$ of the states $|+,\pm\rangle$. This is due to the involvement of transitions at two distinct frequencies, as seen in the right inset, with one twice the other (the general case of a nonzero detuning with three different frequencies involved is considered in Appendix E). Since the dephasing rate Γ_- of the state $|-\rangle$ involves transitions to the two other levels with equal Rabi splitting and thus the interacting phonons have almost the same energy, only one period is observed in the oscillations of Γ_-, analogously to Case A, with vanishing dephasing rate at $d = 0$. In general, $\Gamma_{+,+}$ (consisting of two downwards transitions) will always be greater than $\Gamma_{+,-}$ (two upwards transitions), simply because of spontaneous phonon emission. Furthermore, whether Γ_- or $\Gamma_{+,+}$ is the largest on average depends on the coupling strength chosen. If the Rabi splitting ($\sqrt{2}\bar{g}$) for the transitions contributing to Γ_- is closer to the peak in the phonon spectral density than the energy ($2\sqrt{2}\bar{g}$) of the distant-level transitions included in $\Gamma_{+,-}$, then Γ_- is the largest dephasing rate.

Due to the nature of the hybridized QD-cavity states, the exciton-phonon matrix elements contributing to FGR are now proportional to $V_1 \pm V_2$, with $+$ $(-)$ corresponding to the transitions between distant (neighboring) levels; see Appendix E for details. Since transitions between distant levels contribute to $\Gamma_{+,\pm}$ and thus involve $V_1 + V_2$, there is a nonvanishing contribution even at $d = 0$. This is because the states involved in such transitions both have a cavity contribution, and as cavity does not couple to phonons, the reduction of the dephasing rate to zero is not observed. However, these transition have typically lower impact on decoherence due to the larger phonon energy involved, as discussed in more detail in Appendix E.

V. CONCLUSION

In conclusion, we have presented an asymptotically exact solution for the linear optical response of a system of two coupled qubits interacting with a shared bath, using semiconductor quantum dots coupled to 3D acoustic phonons as illustration. While coupling to the bath causes decoherence, we have shown that the coherence of the bath itself can be exploited to reduce such decoherence. By controlling the distance between the qubits in relation to the wavelength of the interacting bath modes, it is possible to minimize decoherence. This effect is due to all qubits coupled to the same phonon modes and is, a consequence of the coherent properties of the bath. We find that for a 1D bath, decoherence can be eliminated entirely, a case which can also be approached for anisotropic qubits in a 3D bath. This concept can be generalized to multiple-qubit systems.

ACKNOWLEDGMENTS

L.H. acknowledges support from the EPSRC under Grant No. EP/T517951/1. L.S. acknowledges support from the EPSRC under Grant No. EP/R513003/1.

APPENDIX A: EXCITON-PHONON COUPLING ELEMENTS AND PHONON SPECTRAL DENSITY

Throughout this work, we consider semiconductor QDs as candidates for qubits, using typical InGaAs parameters outlined in Refs, [14,15]. At low temperatures, the exciton-phonon interaction is primarily governed by the deformation potential coupling with longitudinal acoustic phonons. Assuming that the phonon parameters within the QDs closely resemble those of the surrounding material, and further assuming that the acoustic phonons exhibit linear dispersion, $\omega_q = v_s q$, where $q = |\mathbf{q}|$ and v_s is the sound velocity in the material, the exciton-phonon coupling matrix element for an exciton in qubit $j = 1, 2$ is given by

$$\lambda_{\mathbf{q},j} = \frac{\sqrt{q}\,\mathcal{D}_j(\mathbf{q})}{\sqrt{2\rho_m v_s \mathcal{V}}}, \tag{A1}$$

where ρ_m is the mass density of the material, $\mathcal{V}$ is the sample volume, and

$$\mathcal{D}_j(\mathbf{q}) = \int d\mathbf{r}_e \int d\mathbf{r}_h |\Psi_{X,j}(\mathbf{r}_e, \mathbf{r}_h)|^2 (D_c e^{i\mathbf{q}\cdot\mathbf{r}_e} - D_v e^{i\mathbf{q}\cdot\mathbf{r}_h}) \tag{A2}$$

is the coupling form factor [14,15], with $D_{c(v)}$ being the deformation potential of the conduction (valence) band. Assuming a factorizable form of the exciton wave functions, $\Psi_{X,j}(\mathbf{r}_e,\mathbf{r}_h)=\psi_{e,j}(\mathbf{r}_e)\psi_{h,j}(\mathbf{r}_h)$, where $\psi_{e(h),j}(\mathbf{r})$ is the confined electron (hole) ground-state wave function in QD j, the form factor simplifies to

$$\mathcal{D}_j(\mathbf{q})=\int d\mathbf{r}[D_c|\psi_{e,j}(\mathbf{r})|^2-D_v|\psi_{h,j}(\mathbf{r})|^2]e^{i\mathbf{q}\cdot\mathbf{r}}. \tag{A3}$$

1. Isotropic quantum dots

Choosing spherically symmetric parabolic confinement potentials, the ground-state wave functions of the carriers take Gaussian form, which in the simpler case of equal electron and hole confinement lengths, $l_{e,j}=l_{h,j}=l_j$, is given by

$$\psi_j(\mathbf{r})=\frac{1}{\pi^{3/4}l_j^{3/2}}\exp\left(-\frac{(\mathbf{r}-\mathbf{d}_j)^2}{2l_j^2}\right), \tag{A4}$$

where $\mathbf{d}_j$ is the coordinate of the center of QD j. Substituting Eq. (A4) into Eq. (A3), performing the integration over the whole space and substituting the result into Eq. (A1), we obtain

$$\lambda_{\mathbf{q},j}=\sqrt{q}\lambda_0\exp\left(-l_j^2q^2/4\right)e^{i\mathbf{q}\cdot\mathbf{d}_j}, \tag{A5}$$

where

$$\lambda_0=\frac{D_c-D_v}{\sqrt{2\rho_m v_s\mathcal{V}}}. \tag{A6}$$

Choosing the first QD located at the origin ($\mathbf{d}_1=0$) we have $\mathbf{d}_2=\mathbf{d}$, where $\mathbf{d}$ is the distance vector between the QDs. Converting the summation over $\mathbf{q}$ to an integration, $\sum_{\mathbf{q}}\to\frac{\mathcal{V}}{(2\pi)^3}\int d\mathbf{q}$, and using spherical coordinates, the spectral density $J_{jj'}(\omega)$ defined by Eq. (20) takes the form

$$J_{jj'}(\omega)=\frac{J_0v_s^4}{2}\int_0^\infty dq\,q^3\exp\{-q^2l^2\}\delta(\omega-v_sq)\times\int_0^\pi d\theta\sin\theta\begin{cases}1 & j=j'\\ \exp\{iqd\cos\theta\} & j<j'\\ \exp\{-iqd\cos\theta\} & j>j'\end{cases}, \tag{A7}$$

where

$$J_0=\frac{(D_c-D_v)^2}{4\pi^2\rho_m v_s^5}, \tag{A8}$$

$d=|\mathbf{d}|$, and $l^2=(l_j^2+l_{j'}^2)/4$ (for brevity omitting the indices j and j' in the new length l introduced). Performing the integration over the polar angle θ, we arrive at

$$J_{jj'}(\omega)=J_0\,\omega^3\exp\left\{-\frac{\omega^2l^2}{v_s^2}\right\}\times\begin{cases}1 & j=j'\\ \mathrm{sinc}\left(\frac{\omega d}{v_s}\right) & j\neq j'\end{cases}, \tag{A9}$$

where $\mathrm{sinc}(x)=\sin(x)/x$.

2. Anisotropic QDs

For anisotropic QDs with in-plane confinement length l_j and perpendicular confinement length $l_{j,\perp}$, the Gaussian ground-state wave functions Eq. (A4) are modified to

$$\psi_j(x,y,z)=\frac{1}{\pi^{3/4}l_jl_{\perp,j}^{1/2}}\exp\left\{-\frac{(x-d_{x,j})^2+(y-d_{y,j})^2}{2l_j^2}\right\}\times\exp\left\{-\frac{(z-d_{z,j})^2}{2l_{\perp,j}^2}\right\}, \tag{A10}$$

where we have again taken the case of identical electron and hole localization lengths, $l_{e,j}=l_{h,j}=l_j$ and $l_{\perp,e,j}=l_{\perp,h,j}=l_{\perp,j}$, and used the components $(d_{x,j},d_{y,j},d_{z,j})$ of the vector $\mathbf{d}_j$. Following the same procedure as for isotropic qubits, we obtain

$$\lambda_{\mathbf{q},j}=\sqrt{q}\lambda_0\exp\left\{-l_j^2\left(q_x^2+q_y^2\right)/4-l_{\perp,j}^2q_z^2/4\right\}e^{i\mathbf{q}\cdot\mathbf{d}_j}. \tag{A11}$$

The above equation is assuming that both QDs have the same anisotropy axis (along z). Assuming further that the centers of the QDs lie on the z axis, so that $d_{x,j}=d_{y,j}=0$ and $d_{z,j}=d_j$, we find in spherical coordinates

$$\lambda_{\mathbf{q},j}=\sqrt{q}\lambda_0\exp\left(-q^2\left(l_j^2\sin^2\theta+l_{\perp,j}^2\cos^2\theta\right)/4+iqd_j\cos\theta\right), \tag{A12}$$

using $q_x=q\sin\theta\cos\phi$, $q_y=q\sin\theta\sin\phi$, and $q_z=q\cos\theta$. The spectral density is then given by

$$J_{jj'}(\omega)=\frac{J_0v_s^4}{2}\int_0^\infty dq\,q^3\delta(\omega-v_sq)\times\int_0^\pi d\theta\sin\theta\exp\{-q^2l^2\sin^2\theta-q^2l_\perp^2\cos^2\theta\}\times\begin{cases}1 & j=j'\\ \exp\{iqd\cos\theta\} & j<j'\\ \exp\{-iqd\cos\theta\} & j>j'\end{cases}, \tag{A13}$$

where $l^2=(l_j^2+l_{j'}^2)/4$ and $l_\perp^2=(l_{\perp,j}^2+l_{\perp,j'}^2)/4$. Performing the integration over the polar angle θ, we obtain

$$J_{jj'}(\omega)=J_0\,\omega^3e^{-q^2l_\perp^2}\times\begin{cases}F\left(0,q\sqrt{l_\perp^2-l^2}\right) & j=j'\\ F\left(\frac{d}{2\sqrt{l_\perp^2-l^2}},q\sqrt{l_\perp^2-l^2}\right) & j\neq j'\end{cases}, \tag{A14}$$

with $q=\omega/v_s$, where

$$F(\alpha,\beta)=\frac{\sqrt{\pi}}{4\beta}[e^{-2i\alpha\beta}w(\alpha-i\beta)-e^{2i\alpha\beta}w(\alpha+i\beta)], \tag{A15}$$

and $w(z)$ is the Faddeeva function. Note that Eq. (A14) is valid for both $l_\perp>l$ and $l_\perp<l$, and in the isotropic case $l_\perp=l$ simplifies to Eq. (A9), as shown in Sec. A 3 below.

3. Faddeeva function and some properties of $F(\alpha,\beta)$

The Faddeeva function $w(z)$ is defined as

$$w(z)=\frac{2}{\sqrt{\pi}}\int_0^\infty e^{2izt}e^{-t^2}dt, \tag{A16}$$

for any complex number z. Physically, it has the meaning of a convolution of Gaussian and complex Lorentzian functions.

In fact, for Im $z > 0$, Eq. (A16) is equivalent to

$$w(z) = \frac{i}{\pi}\int_{-\infty}^{\infty}\frac{e^{-t^2}}{z-t}\,dt. \tag{A17}$$

The Faddeeva function has the properties

$$w(-z) = 2e^{-z^2} - w(z) \quad \text{and} \quad [w(z)]^* = w(-z^*), \tag{A18}$$

and is linked to the error function erf(z) by

$$w(z) = e^{-z^2}[1 + \mathrm{erf}(iz)], \tag{A19}$$

where

$$\mathrm{erf(z)} = \frac{2}{\sqrt{\pi}}\int_0^z \mathrm{e}^{-\mathrm{t}^2}\mathrm{dt}. \tag{A20}$$

It can also be expressed in terms of the Dawson function $D(z)$ as

$$w(z) = e^{-z^2} + \frac{2i}{\sqrt{\pi}}D(z), \tag{A21}$$

where

$$D(z) = \int_0^\infty e^{-t^2}\sin(2zt)dt = e^{-z^2}\int_0^z e^{t^2}dt. \tag{A22}$$

Clearly, all three functions, $w(z)$, erf(iz), and $D(z)$, are equivalent in the sense that they can be expressed by each other. Analytically, the error function has an advantage that it is an entire function, so that $[\mathrm{erf(z)}]^* = \mathrm{erf(z^*)}$, in addition to being an odd function, $\mathrm{erf}(-\mathrm{z}) = -\mathrm{erf(z)}$. However, numerically, the Faddeeva function (as well the Dawson function) is generally more accurate and stable, since the error function erf(z) diverges at large imaginary values of z, but the Faddeeva and Dawson functions do not.

The function $F(\alpha, \beta)$, introduced in Eq. (A15) can also be written as

$$F(\alpha,\beta) = \frac{1}{2}\int_{-1}^{1} e^{\beta^2(1-x^2)}e^{2i\alpha\beta x}dx, \tag{A23}$$

reflecting the integration over the polar angle in Eq. (A13). It has the properties

$$F(\alpha,\beta) = F(-\alpha,\beta) = F(\alpha,-\beta), \tag{A24}$$

which are easy to see by using the definition Eq. (A23) but can be obtained also from the analytic form Eq. (A15) and the properties of the Faddeeva function, Eq. (A18).

For $\alpha = 0$, corresponding to $d = 0$ in Eq. (A14), one has

$$F(0,\beta) = \frac{\sqrt{\pi}}{4}\frac{w(-i\beta) - w(i\beta)}{\beta} = \frac{\sqrt{\pi}}{2}e^{\beta^2}\frac{\mathrm{erf}(\beta)}{\beta} \tag{A25}$$

and in the limit $\beta \to 0$, corresponding to isotropic dots ($l_\perp = l$) or zero-frequency ($q = 0$),

$$\lim_{\beta\to 0} F(0,\beta) = 1, \tag{A26}$$

so that Eq. (A14) simplifies to Eq. (A9).

In the isotropic limit ($l_\perp = l$), $\beta \to 0$ and $\alpha = qd/(2\beta) \to \infty$, and we obtain from Eq. (A15)

$$\lim_{\beta\to 0} F\left(\frac{qd}{2\beta},\beta\right) = -\frac{\sqrt{\pi}}{4}(e^{iqd} - e^{-iqd})\lim_{\beta\to 0}\frac{1}{\beta}w\left(\frac{qd}{2\beta}\right) = \mathrm{sinc}\,(qd)\,, \tag{A27}$$

using

$$\lim_{z\to\infty} zw(z) = \lim_{z\to\infty}\frac{1}{\sqrt{\pi}}\int_0^\infty e^{iz'}\exp\left\{-\frac{z'^2}{2z^2}\right\}dz' = \frac{i}{\sqrt{\pi}} \tag{A28}$$

with z'/z being real, as it follows from the definition Eq. (A16), again, in agreement with Eq. (A9).

Let us finally consider the limit of a strong anisotropy, $l \gg l_\perp$ which is used at the end of Sec. D 2 below. In this limit,

$$\alpha = \frac{d}{2\sqrt{l_\perp^2 - l^2}} \approx \frac{-id}{2l} \quad \text{and} \quad \beta = q\sqrt{l_\perp^2 - l^2} \approx iql, \tag{A29}$$

with $2\alpha\beta = qd$. Under the condition that $|\alpha| \ll |\beta|$ (equivalent to $d \ll 2l^2q$) one can then obtain from Eq. (A15)

$$\begin{aligned} F(0,\beta) - F(\alpha,\beta) &\approx -\frac{\sqrt{\pi}}{4iql}[(1-e^{iqd})w(-ql) - (1-e^{-iqd})w(ql)] \\ &= \frac{\sqrt{\pi}}{4iql}\left[4w(ql)\sin^2\frac{qd}{2} - (1-e^{iqd})e^{-q^2l^2}\right], \end{aligned} \tag{A30}$$

using Eq. (A18). Clearly, this function vanishes if $\sin(qd/2) = 0$. In the case of $ql \gg 1$ this simplifies to just

$$F(0,\beta) - F(\alpha,\beta) \approx \frac{\sqrt{\pi}}{iql}w(ql)\sin^2\frac{qd}{2} \approx \frac{1}{q^2l^2}\sin^2\frac{qd}{2}, \tag{A31}$$

using the limit Eq. (A28).

APPENDIX B: EXPLICIT FORM OF THE MEMORY KERNEL AND THE CUMULANT ELEMENTS

Using the cumulant element $K_{jj'}(s)$ and Eq. (17) allows us to provide an explicit expression for the memory kernel Eq. (24):

$$\begin{aligned} \mathcal{G}_{i_L\ldots i_1 l} = M_{i_1 l}\exp\{&\xi_l\xi_l K_{11}(0) + \eta_l\eta_l K_{22}(0) \\ &+ 2[\xi_{i_1}\xi_l K_{11}(1) + \eta_{i_1}\eta_l K_{22}(1) \\ &+ (\xi_{i_1}\eta_l + \eta_{i_1}\xi_l)K_{12}(1)] + \ldots \\ &+ 2[\xi_{i_L}\xi_l K_{11}(L) + \eta_{i_L}\eta_l K_{22}(L) \\ &+ (\xi_{i_L}\eta_l + \eta_{i_L}\xi_l)K_{12}(L)]\}. \end{aligned} \tag{B1}$$

The above expression is valid for the shared bath. For independent baths, the relevant modification of the tensor $\mathcal{G}_{i_L\ldots i_1 l}$ consists of setting in Eq. (B1) all the mixed terms to zero, since $K_{12}(s) = 0$ according to Eq. (29).

To calculate the cumulant elements Eq. (18), we use the fact that $K_{jj'}(|n-m|)$ depends on the difference $|n-m|$ only and not on both time steps n and m individually. We therefore can find them recursively using the values of the cumulant functions Eq. (22) on the time grid, starting from

$$K_{jj'}(0) = C_{jj'}(\Delta t). \tag{B2}$$

The remaining $s > 0$ cumulant elements are found recursively via

$$K_{jj'}(s) = \frac{1}{2}\Bigg[C_{jj'}((s+1)\Delta t) - (s+1)K_{jj'}(0) - 2\sum_{h=1}^{s-1}(s+1-h)K_{jj'}(h)\Bigg]. \tag{B3}$$

APPENDIX C: CHOOSING THE TIME STEP IN THE TROTTER DECOMPOSITION APPROACH

The energy separation R between the hybridized states determines the timescale

$$\tau_0 = \frac{2\pi}{R}, \tag{C1}$$

which is the period of the corresponding Rabi rotations. In the discretization used in the LN approach described in Sec. III C, this timescale should be much larger than the time step Δt of discretization, $\Delta t \ll \tau_0$. In the cavity-coupled two-qubit system, R can take three different values, and the above condition should be fulfilled for all of them. For example, at zero detuning ($\Omega_1 = \Omega_2 = \Omega_C$), the same coupling to the cavity ($g_1 = g_2 = \bar{g}$), and no dipolar coupling ($g = 0$), the largest energy separation is evaluated as $R = 2\sqrt{2}\bar{g}$; see the inset in Fig. 5. In the case of the dipolar coupled QDs without a cavity, there are only two hybridized states and therefore only one Rabi splitting, evaluated to $R = 2g$ at zero detuning ($\Omega_1 = \Omega_2$). At the same time, the polaron timescale $\tau_{\rm IB}$ is given by [23]

$$\tau_{\rm IB} \approx \frac{\pi\sqrt{l^2 + l_\perp^2}}{v_s} \tag{C2}$$

for anisotropic QDs with in-plane (l) and perpendicular ($l_\perp$) Gaussian lengths. The polaron timescale characterizes the time to form or disperse a polaron cloud following the creation or destruction of an exciton in a QD. The selected time step Δt must be large enough such that for a given number of $L+1$ time steps within the memory kernel, the resulting memory time of $(L+1)\Delta t$ is larger than $\tau_{\rm IB}$. Specifically, the total time considered via the time steps must cover the dynamics of the cumulant $\mathcal{K}_{i_n i_m}$ given by Eq. (17), which is dependent on the cumulant functions C_{11}, C_{12}, and C_{22}, defined in Eq. (22).

Focusing on the cumulant function $C_{11}(t)$, we see from Fig. 6 that $(L+1)\Delta t \geqslant \tau_{\rm IB}$ is in fact sufficient to fully cover the dynamics due to $C_{11}(t)$. In practice, however, one should perform a convergence test for the chosen parameters, to ensure the full memory time is taken into account. In the case of identical QDs, $C_{11}(t) = C_{22}(t)$; otherwise, the larger $\tau_{\rm IB}$ of the two QDs should be used. However since both QD excitons couple to the same phonons, there are extra cumulant elements $K_{12}(s)$ which depend on the distance d separating the QDs. The effect of this distance dependence is the introduction of a delay time before $C_{12}(t)$ starts to change, this can be seen in the inset of Fig. 7. Physically this delay time is due to the time it takes a phonon to travel between the QDs, which is approximately d/v_s. For consistency, we define in the calculations the delay time t_D to be the time at which the change of $C_{12}(t)$ is equal to a half of its minimum value, i.e.,

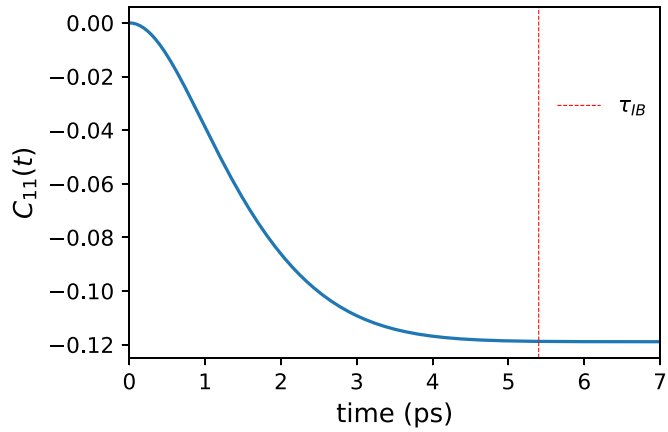

FIG. 6. Temporal evolution of $C_{11}(t)$ (blue line) and the phonon memory time $\tau_{\rm IB}$ (vertical red dashed line). The parameters are as in Fig. 3(c) resulting in $\tau_{\rm IB} = 5.39$ ps.

$C_{12}(t_D) = C_{12}(\infty)/2$. The values of t_D are shown in Fig. 7 (red curve) as a function of the interdot distance, along with its rough estimate d/v_s (red dashed line) working well at large distances.

The presence of the delay time t_D in the cumulant function $C_{12}(t)$ implies that the time step in discretization must be increased to cover the full memory time of $C_{12}(t)$, so the condition $\Delta t = \tau_{\rm IB}/(L+1)$ suitable for a QD-cavity system [23] is no longer sufficient for distant coupled QDs with increasing QD separation d. We therefore modify this condition to

$$\Delta t = \frac{t_D + \tau_{\rm IB}}{L+1}, \tag{C3}$$

which takes the delay time into account, thus covering the memory time for all cumulant elements. The green vertical dashed line in the inset of Fig. 7 demonstrates that all changes

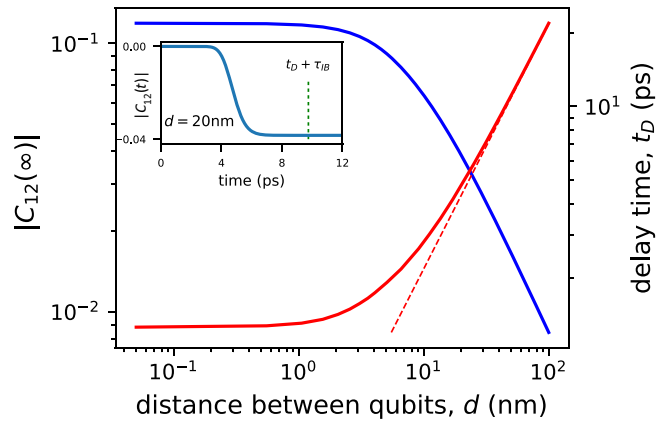

FIG. 7. The asymptotic value of $|C_{12}(t)|$ (blue line, left axis) and the delay time t_D (red line, right axis) as functions of the interdot distance d, with the red dashed line being the estimate d/v_s of the time taken for a phonon to travel between the QDs. The inset shows the temporal evolution of $|C_{12}(t)|$ at $d = 20$ nm, demonstrating the delay time, decay, and saturation at a minimum value. The green vertical dashed line in the inset shows the full memory time considered. The parameters used are the same as in Fig. 6.

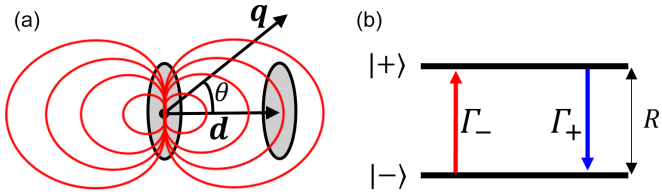

FIG. 8. (a) Schematic of the system of a pair of dipole-dipole coupled anisotropic QDs separated by distance d and a phonon with the wave vector $\mathbf{q}$ emitted or absorbed at an angle θ (for clarity the dipole-dipole interaction is shown only for the left QD acting on the right QD). (b) Nonzero-detuning energy level diagram for the hybridized states $|\pm\rangle$ composed from the basis states $|1\rangle$ and $|2\rangle$ of isolated QDs. Red and blue arrows show phonon-assisted transitions between the hybridized states, resulting in the line broadening Γ_- and Γ_+ of the lower and upper states, respectively.

of the cumulant functions, $C_{ij}(t)$, are covered over the memory time $\Delta t(L+1)$.

As the memory time increases due to the increase in delay time with increasing d, the accuracy of the calculation decreases for a given L due to the increase in time step. As seen from the inset, $C_{12}(t)$ saturates at a minimum value $C_{12}(\infty)$, and the blue line in Fig. 7 shows the decrease of $|C_{12}(\infty)|$ as d increases, implying that $C_{12}(t) \to 0$ as $d \to \infty$. This means in the limit of $d \to \infty$, the full shared phonon bath calculation becomes equivalent to the independent bath case, which is naturally expected, whereby the result is now independent of the distance between the QDs.

APPENDIX D: FERMI'S GOLDEN RULE—DIPOLAR COUPLED QUBITS

In this Appendix, we apply instead of the canonical transformation Eq. (31) used in the main text a unitary transformation to the full Hamiltonian Eq. (1) of the system in Case A, considering two directly coupled QDs without cavity. Following this transformation, we use FGR to calculate the phonon-assisted transition rates between the hybrid QD states, as illustrated in Fig. 8, and consequently the dephasing rates of the linear polarization.

Let us consider the full Hamiltonian $H = H_0 + H_{\rm IB}$, defined in Eqs. (2) and (3) with the cavity coupling $g_1 = g_2 = 0$. In the basis of pure QD states, $|1\rangle$ and $|2\rangle$, H_0 has the following matrix form:

$$H_0 = \begin{pmatrix} \Omega_1 & g \\ g & \Omega_2 \end{pmatrix}. \tag{D1}$$

This matrix can be diagonalized by a unitary transformation $S^\dagger H_0 S = \Lambda$, where

$$S = S^{-1} = S^\dagger = \begin{pmatrix} D_- & D_+ \\ D_+ & -D_- \end{pmatrix}, \tag{D2}$$

with $D_\pm$ given by Eq. (33) and

$$\Lambda = \begin{pmatrix} \Omega_+ & 0 \\ 0 & \Omega_- \end{pmatrix} \tag{D3}$$

being a diagonal matrix of the eigenvalues Eq. (36).

Applying this transformation to the full Hamiltonian, we obtain

$$\begin{aligned} \tilde{H} = S^\dagger H S &= \begin{pmatrix} \Omega_+ & 0 \\ 0 & \Omega_- \end{pmatrix} \\ &+ \begin{pmatrix} D_- & D_+ \\ D_+ & -D_- \end{pmatrix} \begin{pmatrix} V_1 & 0 \\ 0 & V_2 \end{pmatrix} \begin{pmatrix} D_- & D_+ \\ D_+ & -D_- \end{pmatrix} + H_{\rm ph}\mathbb{1} \\ &= \begin{pmatrix} \Omega_+ + V_+ & V \\ V & \Omega_- + V_- \end{pmatrix} + H_{\rm ph}\mathbb{1}, \end{aligned} \tag{D4}$$

with $V_\pm$ defined in the main text and $\mathbb{1}$ being the 2×2 identity matrix. The main outcome of this transformation is the off-diagonal coupling to phonons given by $V = D_+ D_- (V_1 - V_2)$. This coupling is responsible for the phonon-assisted transitions between the hybridized states and ultimately for the long-time dephasing of the optical polarization.

1. Isotropic QDs

Here we evaluate the rate $\Gamma_{\rm ph}$ in FGR Eq. (38) for isotropic QDs, substituting Eq. (A5) into Eq. (39), converting the summation over $\mathbf{q}$ to an integration and further expressing the integration in spherical coordinates, we find

$$\begin{aligned} \Gamma_{\rm ph} = \frac{D_+^2 D_-^2 (D_c - D_v)^2}{8\pi \rho_m v_s} \int_0^\infty dq\, q^3 e^{-q^2 l^2} \\ \times \int_0^\pi d\theta\, \sin\theta (2 - e^{iqd\cos\theta} - e^{-iqd\cos\theta}) \delta(v_s q - R), \end{aligned} \tag{D5}$$

where $l^2 = (l_1^2 + l_2^2)/4$ (for identical QDs $l_1 = l_2 = l\sqrt{2}$). Integrating over θ, we obtain

$$\Gamma_{\rm ph} = \frac{D_+^2 D_-^2 (D_c - D_v)^2}{2\pi \rho_m v_s^5} R^3 e^{-\frac{R^2 l^2}{v_s^2}} \left[1 - \mathrm{sinc}\left(\frac{Rd}{v_s}\right)\right]. \tag{D6}$$

In the case of zero detuning, $R = 2g$ and $D_+ = D_- = 1/\sqrt{2}$. In the limit of $d \to \infty$, $\mathrm{sinc}(Rd/v_s) \to 0$, so that $\Gamma_{\rm ph}$ becomes independent of d. In the limit of $d \to 0$, $\mathrm{sinc}(x) \approx 1 - x^2/6$, leading to a d^2 dependence at small distances and vanishing dephasing rates at $d = 0$.

Let us note also that for a 1D phonon bath which is for example the case of a QD embedded in a quantum wire, the latter providing a 2D quantum confinement of phonon modes, Eq. (39) would give instead, for the same coupling matrix element Eqs. (A1) and (A2) and the linear phonon dispersion $\omega = v_s q$, the following dependence on the Rabi splitting R and interdot distance d:

$$\Gamma_{\rm ph} \propto R\, e^{-\frac{R^2 l_\perp^2}{v_s^2}} \sin^2\left(\frac{Rd}{2v_s}\right), \tag{D7}$$

where $l_\perp$ is the Gaussian length of the electron and hole confinement in the direction of the phonon propagation.

2. Anisotropic QDs

Performing a similar calculation for anisotropic QDs, we find, after substituting the exciton-phonon coupling element

Eq. (A12) into Eq. (39):

$$\Gamma_{\rm ph} = \frac{D_+^2 D_-^2 (D_c - D_v)^2}{8\pi \rho_m v_s} \int_0^\infty dq\, q^3 \times \int_0^\pi d\theta\, \sin\theta e^{-q^2 l^2 \sin^2\theta} e^{-q^2 l_\perp^2 \cos^2\theta} \times (2 - e^{iqd\cos\theta} - e^{-iqd\cos\theta}) \delta(v_s q - R), \quad \text{(D8)}$$

where $l^2 = (l_1^2 + l_2^2)/4$ and $l_\perp^2 = (l_{\perp,1}^2 + l_{\perp,2}^2)/4$ (for identical QDs $l_1 = l_2 = l\sqrt{2}$ and $l_{\perp,1} = l_{\perp,2} = l_\perp\sqrt{2}$). Performing the integration, we obtain

$$\Gamma_{\rm ph} = \frac{D_+^2 D_-^2 (D_c - D_v)^2}{2\pi \rho_m v_s^5} R^3 e^{-q^2 l_\perp^2} \left[F\left(0, q\sqrt{l_\perp^2 - l^2}\right) - F\left(\frac{d}{2\sqrt{l_\perp^2 - l^2}}, q\sqrt{l_\perp^2 - l^2}\right)\right], \quad \text{(D9)}$$

where $q = R/v_s$ and the function $F(\alpha, \beta)$ is given by Eq. (A15).

For strongly anisotropic QDs with $l \gg l_\perp$, $Rl/v_s \gg 1$ (small phonon wavelength) and $d \ll 2l^2 q$ ($|\alpha| \ll |\beta|$), we find using Eq. (A31)

$$\Gamma_{\rm ph} = \frac{D_+^2 D_-^2 (D_c - D_v)^2}{2\pi \rho_m v_s^3} \frac{R}{l^2} e^{-\frac{R^2 l_\perp^2}{v_s^2}} \sin^2\left(\frac{Rd}{2v_s}\right), \quad \text{(D10)}$$

which has the same dependence on the distance d and the Rabi splitting R as in the model of 1D phonons Eq. (D7).

APPENDIX E: FERMI'S GOLDEN RULE—CAVITY-MEDIATED COUPLED QUBITS

Let us now focus on the other special case (Case B) of no direct dipolar coupling of two QD qubits, i.e., $g = 0$, but an indirect coupling mediated by their interaction with a common cavity mode with the coupling constants g_1 and g_2. Reducing the full basis to pure QD states, $|1\rangle$ and $|2\rangle$, and the single-photon cavity state $|C\rangle$, which is sufficient for the linear polarization, the Hamiltonian of the cavity-mediated system takes the form

$$H = H_0 + V_1 |1\rangle\langle 1| + V_2 |2\rangle\langle 2| + H_{\rm ph}, \quad \text{(E1)}$$

where

$$H_0 = \Omega_1 |1\rangle\langle 1| + \Omega_2 |2\rangle\langle 2| + \Omega_C |C\rangle\langle C| + g_1(|1\rangle\langle C| + |C\rangle\langle 1|) + g_2(|2\rangle\langle C| + |C\rangle\langle 2|), \quad \text{(E2)}$$

and $H_{\rm ph}$ and V_i are given by Eq. (4). We apply a transformation diagonalizing H_0 as $S^\dagger H_0 S = \Lambda$, so the full Hamiltonian transforms to

$$\tilde{H} = S^\dagger H S = \mathbb{1} H_{\rm ph} + S^\dagger \begin{pmatrix} \Omega_1 & 0 & g_1 \\ 0 & \Omega_2 & g_2 \\ g_1 & g_2 & \Omega_C \end{pmatrix} S + S^\dagger \begin{pmatrix} V_1 & 0 & 0 \\ 0 & V_2 & 0 \\ 0 & 0 & 0 \end{pmatrix} S, \quad \text{(E3)}$$

where $\mathbb{1}$ is the 3×3 identity matrix. In general, H_0 is diagonalized numerically, providing the hybridized state energy eigenvalues Λ_j. The transformation of the exciton-phonon coupling generates off-diagonal elements responsible for phonon-assisted transition between hybridized QD-cavity states which we account for below using FGR.

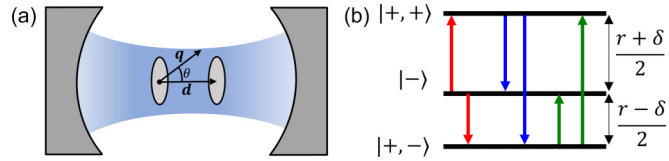

FIG. 9. (a) Schematic of the system of a pair of anisotropic QDs separated by distance d, each interacting independently with the cavity mode and a phonon with the wave vector $\mathbf{q}$ emitted or absorbed at an angle θ. (b) The $g_1 = g_2 = \bar{g}$ and nonzero-detuning ($\delta \neq 0$) energy level diagram for the hybridized states $|+, \pm\rangle$ and $|-\rangle$. These hybridized states are composed from the basis states $|1\rangle$, $|2\rangle$, and $|C\rangle$ of the isolated QDs and the cavity with a single photon. The transitions indicated by the red, blue and green arrows result in the line broadening (dephasing rates) of the central, upper, and lower states, denoted by Γ_-, $\Gamma_{+,+}$, and $\Gamma_{+,-}$, respectively.

Focusing on the analytically solvable case of zero detuning between the QD qubit states, $\Omega_1 = \Omega_2 = \Omega$ (e.g., for identical qubits), and the same coupling of both qubits to the cavity, $g_1 = g_2 = \bar{g}$, the transformation matrix has the following explicit form:

$$S = \begin{pmatrix} d_- & \frac{1}{\sqrt{2}} & d_+ \\ d_- & -\frac{1}{\sqrt{2}} & d_+ \\ \sqrt{2} d_+ & 0 & -\sqrt{2} d_- \end{pmatrix}, \quad \text{(E4)}$$

where

$$d_\pm = \frac{1}{2}\sqrt{1 \pm \frac{\delta}{r}} \quad \text{(E5)}$$

with

$$r = \sqrt{\delta^2 + 8\bar{g}^2} \quad \text{and} \quad \delta = \Omega_C - \Omega, \quad \text{(E6)}$$

the latter being the cavity-QD detuning. The Hamiltonian Eq. (E1) then transforms to

$$\tilde{H} = S^\dagger H S = \mathbb{1} H_{\rm ph} + \begin{pmatrix} \Omega + \frac{\delta + r}{2} + U_+ d_-^2 & \frac{U_- d_-}{\sqrt{2}} & U_+ d_+ d_- \\ \frac{U_- d_-}{\sqrt{2}} & \Omega + \frac{U_+}{2} & \frac{U_- d_+}{\sqrt{2}} \\ U_+ d_+ d_- & \frac{U_- d_+}{\sqrt{2}} & \Omega + \frac{\delta - r}{2} + U_+ d_+^2 \end{pmatrix}, \quad \text{(E7)}$$

where $U_\pm = V_1 \pm V_2$. By applying this transformation, we go from the $|1\rangle$, $|2\rangle$, $|C\rangle$ basis to the hybridized state basis

$$|+, \pm\rangle = d_\mp(|1\rangle + |2\rangle) \pm \sqrt{2} d_\pm |C\rangle, \quad |-\rangle = (|1\rangle - |2\rangle)/\sqrt{2}, \quad \text{(E8)}$$

analogous to that in the polariton transformation of a qubit-cavity system outlined in Ref. [23]. Figure 9 illustrates the level structure of the hybridized states for nonzero detuning ($\delta \neq 0$) and the phonon-assisted transitions due to the off-diagonal elements in Eq. (E7). The rates of these transitions

are estimated below via FGR, similarly to Sec. IV A 2:

$$\Gamma_{\uparrow,\pm} = \mathcal{N}_R \Gamma_{\mathrm{ph},\pm} \quad \text{and} \quad \Gamma_{\downarrow,\pm} = (\mathcal{N}_R + 1)\Gamma_{\mathrm{ph},\pm}, \tag{E9}$$

respectively, for the upwards and downwards transitions, where

$$\Gamma_{\mathrm{ph},\pm} = \pi \sum_q |c_0(\lambda_{\mathbf{q},1} \pm \lambda_{\mathbf{q},2})|^2 \delta(\omega - R). \tag{E10}$$

There are six possible transitions corresponding to the six off-diagonal matrix elements in Eq. (E7). $\mathcal{N}_R$ is the Bose distribution function taken at the energy R, which is the separation of the energy levels of the hybridized states involved in the transition and c_0 is the corresponding factor. These energy levels are given by $\Lambda_{+,\pm} = \Omega + (\delta \pm r)/2$ and $\Lambda_- = \Omega$, according to Eq. (E7). In particular, for $|+,-\rangle \leftrightarrow |-\rangle$ transitions, $R = (r-\delta)/2$ and $c_0 = d_+/\sqrt{2}$; for $|-\rangle \leftrightarrow |+,+\rangle$ transitions, $R = (r+\delta)/2$ and $c_0 = d_-/\sqrt{2}$; finally, for $|+,-\rangle \leftrightarrow |+,+\rangle$ transitions, $R = r$ and $c_0 = d_+ d_-$. Note that for the phonon-assisted transitions between the neighboring levels ($|+,-\rangle \leftrightarrow |-\rangle$ and $|-\rangle \leftrightarrow |+,+\rangle$), the exciton-phonon coupling matrix elements $\lambda_{\mathbf{q},j}$ contribute to Eq. (E10) as a difference due to U_-, thus giving $\Gamma_{\mathrm{ph},-}$, and for transitions between the distant levels ($|+,-\rangle \leftrightarrow |+,+\rangle$) as a sum due to U_+, thus giving $\Gamma_{\mathrm{ph},+}$; see Eq. (E7).

Using the same procedure as in Appendix D, we evaluate the transition rates Eq. (E10) for identical isotropic and anisotropic QD qubits. For isotropic dots, Eq. (E10) yields

$$\Gamma_{\mathrm{ph},\pm} = \frac{c_0^2 (D_c - D_v)^2}{2\pi \rho_m v_s^5} R^3 e^{-\frac{R^2 l^2}{v_s^2}} \left[1 \pm \mathrm{sinc}\left(\frac{Rd}{v_s}\right)\right], \tag{E11}$$

where the difference to Eq. (D6) are the constant factors, the energy distance R, and most importantly the presence of the $\pm$ sign before the sinc function, differentiating the neighboring ($-$) and the distant ($+$) level transitions. Note that the contribution of the distant level transitions to the decoherence is typically less significant due to the factor $e^{-R^2 l^2/v_s^2}$ in which R^2 is four times larger (for zero detuning) than for the neighboring level transitions. Similarly, for anisotropic QDs we find

$$\Gamma_{\mathrm{ph},\pm} = \frac{c_0^2 (D_c - D_v)^2}{2\pi \rho_m v_s^5} R^3 e^{-q^2 l_\perp^2} \left[F\left(0, q\sqrt{l_\perp^2 - l^2}\right) \pm F\left(\frac{d}{4\sqrt{l_\perp^2 - l^2}}, q\sqrt{l_\perp^2 - l^2}\right)\right] \tag{E12}$$

with $q = R/v_s$.

Using Eq. (E11) or Eq. (E12) in combination with Eq. (E9), the contribution to the line broadening for a specific phonon-assisted transition can be found. The line broadening $\Gamma_{+,\pm}$ and Γ_- of the hybridized states is the sum of the broadening by the two available transitions.

APPENDIX F: TRIEXPONENTIAL FIT OF THE POLARIZATION FOR CAVITY-MEDIATED COUPLED QD QUBITS

We show in Fig. 10 the optical linear polarization $|P_{11}(t)|$ for Case B in the main text. The linear polarization (blue dots) for cavity-coupled QD qubits again starts from unity due to the excitation and measurement of the same QD state and has the temporal oscillations now at three frequencies due to addition of a cavity mode. We apply a complex triexponential fit (red curve) of the form $\sum_j C_j e^{-i\omega_j t}$, extracting the complex amplitudes C_j, energies $\mathrm{Re}\,\omega_j$, and dephasing rates $\Gamma_j = -\mathrm{Im}\,\omega_j$ of the phonon-dressed hybridized states. The fit is applied after the phonon-memory cutoff (dashed green vertical line),

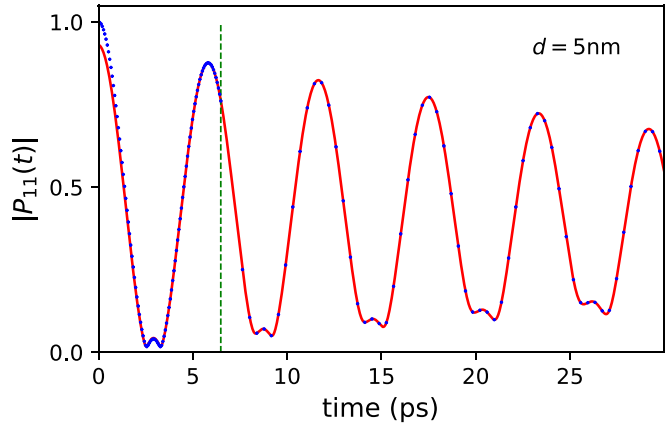

FIG. 10. Linear optical polarization $|P_{11}(t)|$ (blue dots) and its complex triexponential fit (red lines) for cavity-mediated coupled anisotropic QD qubits at zero detuning, separated by a distance $d = 5$ nm, with excitation and measurement in QD 1. The parameters are as in Fig. 5.

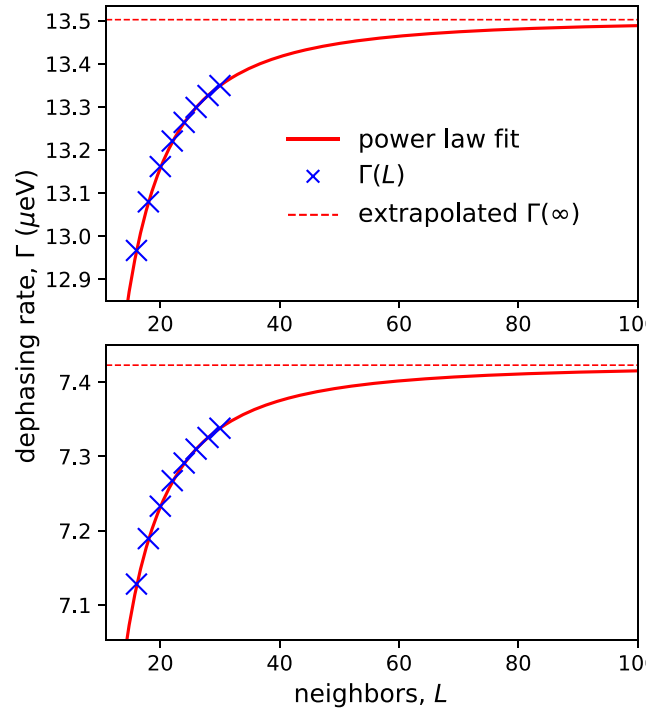

FIG. 11. Power-law fit applied to the $\Gamma_+(L)$ [$\Gamma_-(L)$] values across a range of neighbors, L, for $d = 5$ nm is shown in the upper (lower) figure. The blue crosses are the extracted $\Gamma(L)$ values, the red curve is the power-law model with $\beta = 2$, and the red horizontal dashed line is the estimated value of $\Gamma(\infty)$. The parameters are as in Fig. 3(b).

beyond the polaron cloud formation time. The dephasing rates are then extracted across a range of distances, providing Fig. 5 of the main text.

APPENDIX G: EXTRAPOLATION OF FIT PARAMETERS

As detailed in the main text, Figs. 3 and 5 are created by calculating the linear optical polarization for a given number of neighbors (L), then applying a fit to the long-time data and extracting the fit parameters. The parameters corresponding to the line broadening, $\Gamma(L)$, are extracted across a range of neighbors, and the convergence of $\Gamma(L)$ to the exact ($L = \infty$) value is assumed to follow a power-law model, given by:

$$\Gamma(L) = \Gamma(\infty) + CL^{-\beta}. \tag{G1}$$

Figure 11 shows the $\Gamma(L)$ calculated values (blue crosses) for directly coupled QD qubits treated in Case A, with the power-law model applied (red curve), and the extrapolated $\Gamma(\infty)$ is shown as a red dashed line. The value of $\Gamma(\infty)$ is estimated for the eight values of $\Gamma(L)$ shown in Fig. 11, by minimizing the root-mean-square deviation from the power law Eq. (G1) for $\beta = 2$.

[1] J. Majer, J. M. Chow, J. M. Gambetta, J. Koch, B. R. Johnson, J. A. Schreier, L. Frunzio, D. I. Schuster, A. A. Houck, A. Wallraff, A. Blais, M. H. Devoret, S. M. Girvin, and R. J. Schoelkopf, Coupling superconducting qubits via a cavity bus, Nature (London) **449**, 443 (2007).

[2] A. Imamoglu, D. D. Awschalom, G. Burkard, D. P. DiVincenzo, D. Loss, M. Sherwin, and A. Small, Quantum information processing using quantum dot spins and cavity QED, Phys. Rev. Lett. **83**, 4204 (1999).

[3] M. Delbecq, L. Bruhat, J. Viennot, S. Datta, A. Cottet, and T. Kontos, Photon-mediated interaction between distant quantum dot circuits, Nat. Commun. **4**, 1400 (2013).

[4] G. Massimo Palma, K.-A. Suominen, and A. K. Ekert, Quantum computers and dissipation, Proc. R. Soc. Lond. Ser. A **452**, 567 (1996).

[5] M. Schlosshauer, Quantum decoherence, Phys. Rep. **831**, 1 (2019).

[6] P. Zanardi and M. Rasetti, Noiseless quantum codes, Phys. Rev. Lett. **79**, 3306 (1997).

[7] D. A. Lidar, I. L. Chuang, and K. B. Whaley, Decoherence-free subspaces for quantum computation, Phys. Rev. Lett. **81**, 2594 (1998).

[8] E. B. Flagg, A. Muller, S. V. Polyakov, A. Ling, A. Migdall, and G. S. Solomon, Interference of single photons from two separate semiconductor quantum dots, Phys. Rev. Lett. **104**, 137401 (2010).

[9] R. B. Patel, A. J. Bennett, I. Farrer, C. A. Nicoll, D. A. Ritchie, and A. J. Shields, Two-photon interference of the emission from electrically tunable remote quantum dots, Nat. Phot. **4**, 632 (2010).

[10] L. Zhai, G. N. Nguyen, C. Spinnler, J. Ritzmann, M. C. Löbl, A. D. Wieck, A. Ludwig, A. Javadi, and R. J. Warburton, Quantum interference of identical photons from remote GaAs quantum dots, Nat. Nanotechnol. **17**, 829 (2022).

[11] V. Giesz, S. L. Portalupi, T. Grange, C. Antón, L. De Santis, J. Demory, N. Somaschi, I. Sagnes, A. Lemaître, L. Lanco, A. Auffèves, and P. Senellart, Cavity-enhanced two-photon interference using remote quantum dot sources, Phys. Rev. B **92**, 161302(R) (2015).

[12] P. Borri, W. Langbein, S. Schneider, U. Woggon, R. L. Sellin, D. Ouyang, and D. Bimberg, Ultralong dephasing time in InGaAs quantum dots, Phys. Rev. Lett. **87**, 157401 (2001).

[13] B. Krummheuer, V. M. Axt, and T. Kuhn, Theory of pure dephasing and the resulting absorption line shape in semiconductor quantum dots, Phys. Rev. B **65**, 195313 (2002).

[14] E. A. Muljarov and R. Zimmermann, Dephasing in quantum dots: Quadratic coupling to acoustic phonons, Phys. Rev. Lett. **93**, 237401 (2004).

[15] E. A. Muljarov, T. Takagahara, and R. Zimmermann, Phonon-induced exciton dephasing in quantum dot molecules, Phys. Rev. Lett. **95**, 177405 (2005).

[16] M. Glässl, A. M. Barth, and V. M. Axt, Proposed robust and high-fidelity preparation of excitons and biexcitons in semiconductor quantum dots making active use of phonons, Phys. Rev. Lett. **110**, 147401 (2013).

[17] J. H. Quilter, A. J. Brash, F. Liu, M. Glässl, A. M. Barth, V. M. Axt, A. J. Ramsay, M. S. Skolnick, and A. M. Fox, Phonon-assisted population inversion of a single InGaAs/GaAs quantum dot by pulsed laser excitation, Phys. Rev. Lett. **114**, 137401 (2015).

[18] M. Reindl, K. D. Jöns, D. Huber, C. Schimpf, Y. Huo, V. Zwiller, A. Rastelli, and R. Trotta, Phonon-assisted two-photon interference from remote quantum emitters, Nano Lett. **17**, 4090 (2017).

[19] T. Grange, N. Somaschi, C. Antón, L. De Santis, G. Coppola, V. Giesz, A. Lemaître, I. Sagnes, A. Auffèves, and P. Senellart, Reducing phonon-induced decoherence in solid-state single-photon sources with cavity quantum electrodynamics, Phys. Rev. Lett. **118**, 253602 (2017).

[20] A. Morreau, C. Joshi, and E. A. Muljarov, Phonon-induced dephasing inquantum dot-cavity QED: Limitations of the polaron master equation, arXiv:2002.01912.

[21] L. S. Sirkina and E. A. Muljarov, Impact of the phonon environment on the nonlinear quantum-dot–cavity QED: Path-integral approach, Phys. Rev. B **108**, 115312 (2023).

[22] I. Wilson-Rae and A. Imamoglu, Quantum dot cavity-QED in the presence of strong electron-phonon interactions, Phys. Rev. B **65**, 235311 (2002).

[23] A. Morreau and E. A. Muljarov, Phonon-induced dephasing in quantum-dot–cavity QED, Phys. Rev. B **100**, 115309 (2019).

[24] P. Zanardi and F. Rossi, Quantum information in semiconductors: Noiseless encoding in a quantum-dot array, Phys. Rev. Lett. **81**, 4752 (1998).

[25] A. O. Govorov, Spin-Förster transfer in optically excited quantum dots, Phys. Rev. B **71**, 155323 (2005).

[26] E. Rozbicki and P. Machnikowski, Quantum kinetic theory of phonon-assisted excitation transfer in quantum dot molecules, Phys. Rev. Lett. **100**, 027401 (2008).

[27] A. Thilagam and M. A. Lohe, Decoherence of excitonic qubits in Förster coupled quantum dots, J. Phys.: Condens. Matter **20**, 315205 (2008).

[28] D. Gribben, A. Strathearn, J. Iles-Smith, D. Kilda, A. Nazir, B. W. Lovett, and P. Kirton, Exact quantum dynamics in structured environments, Phys. Rev. Res. **2**, 013265 (2020).

[29] S. Reitzenstein, A. Löffler, C. Hofmann, A. Kubanek, M. Kamp, J. P. Reithmaier, A. Forchel, V. D. Kulakovskii, L. V. Keldysh, I. V. Ponomarev, and T. L. Reinecke, Coherent photonic coupling of semiconductor quantum dots, Opt. Lett. **31**, 1738 (2006).

[30] F. Albert, K. Sivalertporn, J. Kasprzak, M. Strauß, C. Schneider, S. Höfling, M. Kamp, A. Forchel, S. Reitzenstein, E. Muljarov, and W. Langbein, Microcavity controlled coupling of excitonic qubits, Nat. Commun. **4**, 1747 (2013).

[31] D. J. van Woerkom, P. Scarlino, J. H. Ungerer, C. Müller, J. V. Koski, A. J. Landig, C. Reichl, W. Wegscheider, T. Ihn, K. Ensslin, and A. Wallraff, Microwave photon-mediated interactions between semiconductor qubits, Phys. Rev. X **8**, 041018 (2018).

[32] F. Grosse, E. A. Muljarov, and R. Zimmermann, Phonons in quantum dots and their role in exciton dephasing, in *Semiconductor Nanostructures*, edited by P. Avouris, B. Bhushan, D. Bimberg, K. Von Klitzing, H. Sakaki, R. Wiesendanger, and D. Bimberg (Springer, Berlin, 2008), pp. 165–187.

[33] G. D. Mahan, *Many-Particle Physics* (Springer US, Boston, MA, 2000).

[34] L. S. Sirkina, L. M. J. Hall, A. Morreau, W. Langbein, and E. A. Muljarov, Förster transfer between quantum dots in a shared phonon environment: A rigorous approach, revealing the role of puredephasing (unpublished).

[35] P. Machnikowski, Change of decoherence scenario and appearance of localization due to reservoir anharmonicity, Phys. Rev. Lett. **96**, 140405 (2006).

[36] J. I. Climente, A. Bertoni, G. Goldoni, and E. Molinari, Phonon-induced electron relaxation in weakly confined single and coupled quantum dots, Phys. Rev. B **74**, 035313 (2006).

[37] P. Nalbach, J. Eckel, and M. Thorwart, Quantum coherent biomolecular energy transfer with spatially correlated fluctuations, New J. Phys. **12**, 065043 (2010).

[38] P. Kumar, C. Jennings, M. Scheibner, A. S. Bracker, S. G. Carter, and D. Gammon, Spectral broadening of optical transitions at tunneling resonances in InAs/GaAs coupled quantum dot pairs, Phys. Rev. B **102**, 085423 (2020).

[39] V. N. Stavrou, Spin qubits: Spin relaxation in coupled quantum dots, J. Phys.: Condens. Matter **30**, 455301 (2018).

[40] G. Lindwall, A. Wacker, C. Weber, and A. Knorr, Zero-phonon linewidth and phonon satellites in the optical absorption of nanowire-based quantum dots, Phys. Rev. Lett. **99**, 087401 (2007).

[41] V. Ardizzone, Y. Chassagneux, F. Vialla, G. Delport, C. Delcamp, N. Belabas, E. Deleporte, Ph. Roussignol, I. Robert-Philip, C. Voisin, and J. S. Lauret, Strong reduction of exciton-phonon coupling in single-wall carbon nanotubes of high crystalline quality: Insight into broadening mechanisms and exciton localization, Phys. Rev. B **91**, 121410(R) (2015).

[42] A. Jeantet, Y. Chassagneux, T. Claude, P. Roussignol, J. S. Lauret, J. Reichel, and C. Voisin, Exploiting one-dimensional exciton–phonon coupling for tunable and efficient single-photon generation with a carbon nanotube, Nano Lett. **17**, 4184 (2017).

[43] S. Lüker, T. Kuhn, and D. E. Reiter, Phonon impact on optical control schemes of quantum dots: The role of quantum dot geometry and symmetry, Phys. Rev. B **96**, 245306 (2017).

[44] P. Zanardi and F. Rossi, Subdecoherent information encoding in a quantum-dot array, Phys. Rev. B **59**, 8170 (1999).